

QUARTERLY JOURNAL  
OF THE  
ROYAL METEOROLOGICAL SOCIETY

Vol. 129

JULY 2003 Part A

No. 592

*Q. J. R. Meteorol. Soc.* (2003), **129**, pp. 2089–2116

doi: 10.1256/qj.01.208

Characteristics of mixed-phase clouds. I: Lidar, radar and aircraft observations  
from CLARE'98

By R. J. HOGAN<sup>1</sup>\*, P. N. FRANCIS<sup>2</sup>, H. FLENTJE<sup>3</sup>,  
A. J. ILLINGWORTH<sup>1</sup>, M. QUANTE<sup>4</sup> and J. PELON<sup>5</sup>

<sup>1</sup>*Department of Meteorology, University of Reading, UK*

<sup>2</sup>*Met Office, UK*

<sup>3</sup>*DLR, Oberpfaffenhofen, Germany*

<sup>4</sup>*GKSS Forschungszentrum, Geesthacht, Germany*

<sup>5</sup>*Université Pierre et Marie Curie, CNRS-IPSL, Paris, France*

(Received 19 December 2001; revised 19 December 2002)

SUMMARY

Results are presented from two case-studies during the 1998 Cloud Lidar And Radar Experiment (CLARE'98) in which mixed-phase clouds were observed by a multitude of ground-based and airborne instruments. In both cases supercooled liquid water was present in the form of highly reflective layers in lidar imagery, while the radar echo was dominated by the contribution from the much larger ice particles. In the first case-study, four individual liquid-water layers were observed by an airborne nadir-pointing polarimetric lidar at temperatures between  $-7^{\circ}\text{C}$  and  $-15^{\circ}\text{C}$ , embedded within a warm-frontal ice cloud. Their phase was confirmed by the *in situ* measurements and by their very low depolarization of the lidar signal. The effective droplet radius ranged from 2 to  $5\ \mu\text{m}$ . Simultaneous temperature and vertical-wind measurements by the aircraft demonstrated that they were generated by a gravity wave with a wavelength of around 15 km. Thin sector plates grew rapidly in the high-supersaturation conditions and were responsible for the high values of differential reflectivity measured by the ground-based radar in the vicinity of the layers. In the second case-study a liquid-water altocumulus layer was observed at  $-23^{\circ}\text{C}$ , which was slowly glaciating. Profiles of liquid and ice extinction coefficient, water content and effective radius were derived from the remote measurements taken in both cases, using radar–lidar and dual-wavelength radar techniques to size the ice particles; where *in situ* validation was available, agreement was good. Radiative-transfer calculations were then performed on these profiles to ascertain the radiative effect of the supercooled water. It was found that, despite their low liquid-water path (generally less than  $10\text{--}20\ \text{g m}^{-2}$ ), these clouds caused a significant increase in the reflection of solar radiation to space, even when cirrus was present, above which the long-wave signal dominated. In the cases considered, their capacity to decrease the net absorbed radiation was at least twice as large as that of the ice. The layers were typically 100–200 m thick, suggesting that they are unlikely to be adequately represented by the resolutions of current forecast and climate models. These results suggest that a spaceborne lidar and radar would be ideally suited to characterizing the occurrence and climatological importance of mixed-phase clouds on a global scale.

KEYWORDS: Depolarization ratio Radar–lidar synergy Radiative effect Supercooled water

1. INTRODUCTION

Of primary importance in determining the radiative properties and evolution of a cloud is its phase. Mixed-phase clouds have the potential to play an important role in the climate system (Li and Le Treut 1992; Sun and Shine 1995; Gregory and Morris 1996),

\* Corresponding author: Department of Meteorology, Earley Gate, PO Box 243, Reading, Berkshire RG6 6BB, UK.  
e-mail: r.j.hogan@reading.ac.uk

© Royal Meteorological Society, 2003. P. N. Francis's contribution is Crown copyright.

but due to a lack of good observational datasets there is much uncertainty regarding the extent to which ice and liquid water coexist, and how to represent the ice-to-liquid-water ratio below 0 °C in forecast and climate models. Intuitively one might expect microscale coexistence of the two phases to be rare in stratiform clouds, since such a situation is inherently unstable with the ice particles able to grow rapidly at the expense of the liquid-water droplets by virtue of the difference in saturation vapour pressure (the 'Bergeron–Findeison' mechanism). There is clearly a need for observations to improve our understanding of both the important microphysical processes that act in mixed-phase clouds and the resulting macroscale distribution of ice and liquid water. Aircraft measurements have been used to provide useful statistics on mixed-phase clouds (e.g. Moss and Johnson 1994; Bower *et al.* 1996), but to get an idea of the overall cloud morphology requires high-resolution (i.e. around 100 m) remote-sensing techniques that have the ability to distinguish liquid water from ice.

One of the most promising methods to emerge in the last two decades has been the polarization lidar technique; non-spherical ice particles can be distinguished from liquid-water droplets because they depolarize the incident light (see the review by Sassen (1991)). Eberhard (1995) proposed the use of dual-wavelength carbon-dioxide lidar, which utilizes the fact that the ratio of backscatter coefficient at suitably separated wavelengths is different for liquid droplets and ice particles. The main limitation of ground-based lidars is that they are strongly attenuated by intervening boundary-layer liquid-water clouds, so while they are useful for studying altocumulus and mixed-phase orographic clouds (e.g. Sassen 1984; Sassen *et al.* 1990; Heymsfield *et al.* 1991; Wylie *et al.* 1995), they cannot be used from the ground to study the mixed-phase regions of precipitating frontal systems, which invariably have an optical depth of more than 2 or 3.

In this paper we use observations by two airborne polarimetric lidars and thus circumvent the problem of penetrating the thick low-level cloud. This makes the results particularly relevant for planned and proposed spaceborne lidars. It is shown that the combination of radar and lidar offers a straightforward way to infer the presence of supercooled liquid water in stratiform clouds. Because of the vastly larger concentration of cloud condensation nuclei than ice nuclei in the atmosphere, when supercooled water clouds are formed the available liquid water is distributed amongst a large number of small droplets, while ice particles are typically larger and much less numerous. Since at lidar wavelengths cloud particles scatter in the geometric optics regime, the backscattered intensity is approximately proportional to the square of particle diameter, and so large numbers of small liquid-water droplets can easily dominate the signal when they are present. Conversely, the radar operates in or close to the Rayleigh scattering regime, and the echo power is approximately proportional to the square of particle mass. Thus, the radar reflectivity factor ( $Z$ ), and other radar parameters such as differential reflectivity ( $Z_{DR}$ ) are always dominated by the larger ice particles, even when liquid water is present. It is found that supercooled liquid water is strikingly visible to the lidar as thin but highly reflective layers, and in the companion paper to this by Hogan *et al.* (2003) an algorithm is used to objectively identify such layers in a three-year dataset from an unpolarized ground-based lidar, and characterize their occurrence as a function of temperature. An interesting microphysical effect of the layers is that they appear to cause ice crystals to grow into columns or plates (depending on the temperature) with extreme axial ratios, which are then detected by the radar as regions of unusually high  $Z_{DR}$ . This phenomenon was explored in detail by Hogan *et al.* (2002).

The data used in this paper were taken during the 1998 Cloud Lidar And Radar Experiment (CLARE'98). Section 2 outlines the capabilities of the ground-based and

airborne instruments used in the experiment, and in sections 3 and 4 we describe the two case-studies in which mixed-phase clouds were observed. Then in section 5 a one-dimensional radiation model is used to estimate the radiative effect of the supercooled liquid-water layers, using realistic profiles of liquid- and ice-water content and effective radius retrieved from the remote measurements made in the two case-studies. We use both the radar–lidar backscatter ratio and the ratio of radar reflectivities measured at 35 and 94 GHz to estimate ice-particle size, techniques which have also been proposed for use from space (ESA 1999b; Hogan and Illingworth 1999). Some *in situ* validation is also presented.

## 2. THE 1998 CLOUD LIDAR AND RADAR EXPERIMENT

The CLARE'98 campaign took place at Chilbolton, England, between 5 and 23 October 1998, funded by the European Space Agency (ESA) to support the development of retrieval algorithms for a future spaceborne cloud radar and lidar. Details of the many ground-based and airborne instruments that were involved may be found in ESA (1999a). In this paper we present observations from two of the seven CLARE'98 flights. The three aircraft flew co-ordinated runs towards and away from Chilbolton along the 260° azimuth. The Deutsches Zentrum für Luft- und Raumfahrt (DLR) Falcon aircraft flew at an altitude of around 13 km and observed the cloud from above with its nadir-viewing polarimetric 'ALEX' lidar. Meanwhile the French Avion de Recherche Atmosphérique et de Télédétection (ARAT) flew at an altitude of around 5 km and observed the clouds with its polarimetric Leandre lidar and 94 GHz Kestrel cloud radar (although Kestrel data are not used in this paper). The UK Met Office C-130 aircraft then made *in situ* measurements of the cloud with its comprehensive array of microphysical probes. During the runs the ground-based 3 GHz Chilbolton Advanced Meteorological Radar (CAMRa) performed scans along the 260° azimuth. The inbound overhead times of the aircraft were synchronized, and at the end of each inbound run and start of each outbound run the clouds were also observed by three vertically pointing cloud radars and a 905 nm Vaisala CT75K lidar ceilometer (used extensively by Hogan *et al.* 2003) on the ground at Chilbolton. These instruments are now described in more detail.

### (a) Airborne-lidar observations

The ALEX lidar on board the Falcon aircraft makes use of an Nd:YAG laser to provide measurements of attenuated backscatter coefficient ( $\beta'$ ) at 1024, 532 and 355 nm. In addition to the cloud return, the shorter wavelengths are able to detect molecular scattering, thus providing a means of absolute calibration as well as the possibility of measuring optical depth using the molecular return from the far side of the cloud. This can then be used to correct the measured  $\beta'$  values for attenuation, provided of course that the molecular echo is not so attenuated that it cannot be detected. A depolarization channel is also available at 532 nm, providing information on the phase of the target hydrometeors. The performance of the system was described fully by Mörl *et al.* (1981). The Falcon flew at around twice the speed of the other aircraft, so flew longer runs to ensure synchronization of the overhead times.

The specification of the Leandre lidar on the ARAT aircraft is rather similar to that of ALEX, and is described by Pelon *et al.* (1990). It can be pointed either at nadir or zenith. Unfortunately the ARAT had a flight ceiling of around 5.5 km, and in the first case-study was not able to fly above cloud top so only the base of the cloud was observed from its location within the cloud. In the second case-study (section 4) it flew below the cloud of interest and was able to make lidar measurements from beneath.

(b) *Ground-based radar observations*

The scanning 3 GHz radar has an antenna diameter of 25 m, a beam width of  $0.28^\circ$  and full Doppler and polarization capability; details may be found in Goddard *et al.* (1994b). During most of the outbound runs a slow but variable-speed vertical scan was performed to maximize collocation of the data by attempting to keep the C-130 in or close to the radar beam. On many occasions the C-130 was 'hit' by the radar, and in a few cases it was visible through most of the duration of a 5 min scan, a considerable achievement given the narrowness of the beam. The radar is calibrated to 0.5 dB using the technique of Goddard *et al.* (1994a).

Three ground-based cloud radars were used in combination with the airborne lidars to retrieve profiles of cloud properties for input into a one-dimensional radiation model (see section 5). The permanent Chilbolton 94 GHz Galileo radar and the transportable 95 GHz Miracle radar of the GKSS Institute for Atmospheric Physics in Germany (Quante *et al.* 1998) were both operated continuously at zenith. The 35 GHz Rabelais radar, on loan from the University of Toulouse, was mounted on the side of the main 25 m dish to permit scanning with CAMRa, which meant that it was not always at vertical at the times of the aircraft over-flights of Chilbolton. During the over-flights the Miracle radar switched to an operational mode that permitted recording of the full Doppler spectrum of particle fall velocities, but which limited the sampling window to a 2.5 km range enclosing the height of the C-130.

The cloud radars were calibrated by comparison with the CAMRa system; firstly the 3 GHz and 35 GHz radars were matched up while scanning through light, Rayleigh-scattering rain, and then the Galileo and Miracle were compared with the Rabelais while dwelling vertically in thin low-level liquid-water cloud (for details see Hogan and Goddard 1999). Correction for attenuation by atmospheric gases was performed using the line-by-line model of Liebe (1985) together with temperature and humidity profiles from the mesoscale version of the Met Office Unified Model. The model dataset is comprised of the 6-hourly analyses and the intervening hourly forecasts, and is also used to estimate the horizontal wind along the aircraft tracks in sections 3(a) and 4. Liquid-water attenuation can also be a problem at 94 GHz, but the profiles analysed in section 5 were from occasions with no low cloud present. The liquid-water path of the supercooled clouds was generally less than  $10 \text{ g m}^{-2}$  (see section 5), which at  $-15^\circ \text{C}$  would cause a two-way 94 GHz attenuation of only around 0.08 dB, so can be neglected. Ice attenuation is negligible at these frequencies (Hogan and Illingworth 1999).

(c) *The UK Met Office C-130 aircraft*

The Met Office C-130 Hercules carried a comprehensive array of microphysical probes suitable for characterizing mixed-phase clouds. Bulk ice-water content (IWC) was estimated by integrating size spectra derived from two imaging probes: the two-dimensional (2D) cloud (2D-C) and 2D precipitation (2D-P) probes measured hydrometeors in the diameter ranges 25–800  $\mu\text{m}$  and 200–6400  $\mu\text{m}$  respectively, and are based on the instrument described by Knollenberg (1970). The mass–area relationship of Francis *et al.* (1998) was used in order to minimize the differences with IWC derived using the evaporative technique of Brown (1993). Bulk liquid-water content (LWC) was provided by a Johnson-Williams hot-wire probe. The Forward Scattering Spectrometer Probe (FSSP) counts particles in the diameter range 2–47  $\mu\text{m}$ , although because over-counting may occur when large ice particles are present (Gardiner and Hallett 1985) we use only the effective droplet radius reported by this instrument. The distribution is

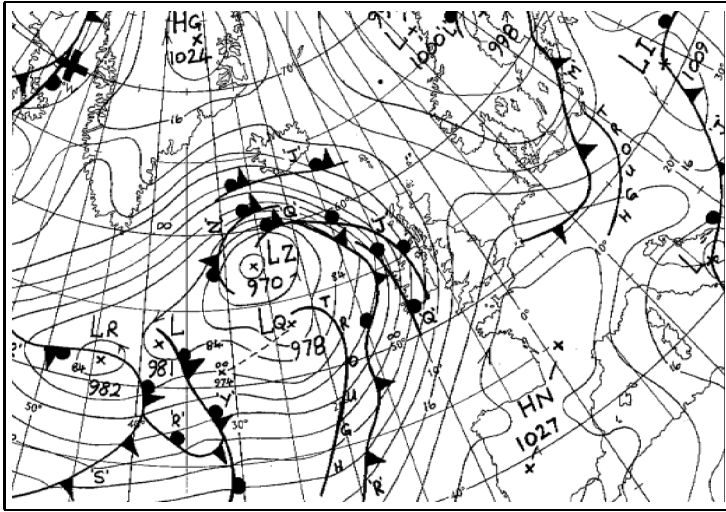


Figure 1. UK Met Office surface analysis at 1200 UTC on 20 October 1998.

truncated at a diameter of  $30 \mu\text{m}$  to minimize ice contamination, although this generally changes effective radius by less than 10%.

### 3. 20 OCTOBER 1998 CASE-STUDY

#### (a) Synopsis

On 20 October 1998 a warm front swept across the UK from the south-west, ahead of which there was extensive cloud at all heights. The Met Office surface analysis from 1200 UTC is shown in Fig. 1. Low-level stratocumulus was present intermittently through most of the day, but from 1300 UTC to around 1600 UTC midlevel cloud was also present between 2 km and 6 km. Figure 2 shows the 1503 UTC infrared satellite image (a) and the 1400 UTC Larkhill radiosonde ascent (b), in which it can be seen that at temperatures between around  $-8^\circ\text{C}$  and  $-16^\circ\text{C}$ , the air was close to saturation with respect to liquid water. Larkhill is located 25 km to the west of Chilbolton, and at the nearest point is only 10 km from the  $260^\circ$  azimuth aircraft flight track.

We start by describing the observations made during the inbound run leading up to the 1420 UTC over-flight of Chilbolton, in which supercooled water was observed by both the ALEX lidar (in the form of highly reflective layers) and the *in situ* probes, and indirect evidence for it obtained from radar. In fact, highly reflective layers were observed by ALEX in numerous previous runs, but the C-130 had not been at the correct altitude to provide *in situ* validation. After 1430 UTC the layers either dissipated or were advected out of the flying area and liquid water was no longer detected by the *in situ* measurements. The Falcon performed one last outbound run before returning home.

A composite of the measurements of the C-130 aircraft, the Falcon aircraft and the 3 GHz radar from the inbound run leading up to the 1420 UTC over-flight is shown in Fig. 3. To account for the non-coincidence of the measurements in time (because the Falcon flew at around twice the speed of the other aircraft), the data from each instrument were displaced using the component of the wind along the flight track at the altitude of the C-130 aircraft, such that each should represent a 'snap shot' of the clouds at the instant that the scanning radar reached zenith. According to the Unified Model, the

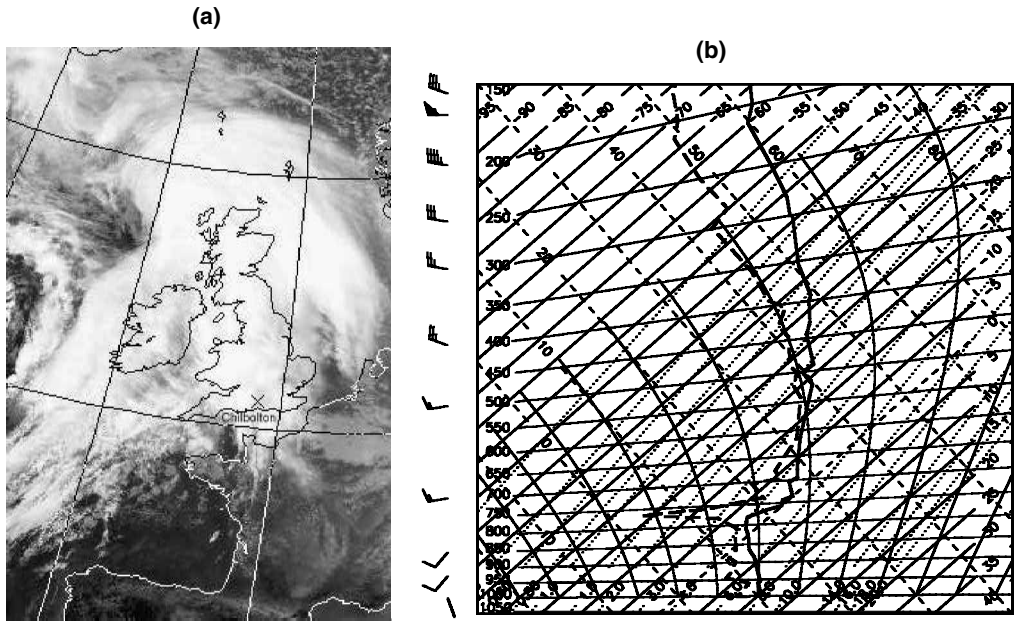


Figure 2. (a) Satellite infrared image at 1503 UTC, 20 October 1998, and (b) a tephigram of the Larkhill radiosonde ascent at 1400 UTC.

wind during this run was  $20 \text{ m s}^{-1}/258^\circ$  at the altitude of the C-130,  $2^\circ$  from the azimuth along which the aircraft were flying as they approached the radar. Similar values were measured by the radar itself at this altitude. The vector change in wind velocity over the 3–6 km height range where the midlevel cloud occurred was around  $5 \text{ m s}^{-1}$ . The maximum time offset between instruments in Fig. 3 was at 60 km from Chilbolton, where the Falcon lidar sampled the cloud 4.5 min earlier than the C-130.

### (b) Comparison of lidar and radar observations

Figure 3(a) depicts attenuated backscatter coefficient ( $\beta'$ ) at 1064 nm as measured by the nadir-pointing ALEX lidar on board the DLR Falcon aircraft. Cirrus is present between 9.5 km and 12.5 km, and the strong depolarization of the signal (up to 50%) in the next panel confirms that this cloud was composed entirely of non-spherical ice particles. The midlevel cloud beneath, however, appears to have thin layers of high  $\beta'$ , around 150 m thick, embedded within it at four different altitudes. The temperature of the highest layer (at an altitude of 5.8 km) was around  $-15^\circ \text{C}$ , and coincides with the near-saturated layer in the radiosonde profile. The low depolarization of these layers, shown in the second panel, indicates that they were composed of spherical supercooled liquid-water droplets. Figure 3(c) shows  $Z$  as measured by the scanning 3 GHz radar, in which there is absolutely no sign of the layers that were so obvious in the lidar signal; the radar signal is dominated by the larger but far less numerous ice particles. This indicates that the layers were composed of particles much smaller but much more numerous than the ice particles, further evidence that they were liquid-water droplets.

The airborne lidar signal was attenuated significantly by the upper layers such that the full extent of the lowest layer at 4 km was not revealed. Between 1355 UTC and 1420 UTC (i.e. during this aircraft run) a gap in the stratocumulus at 2 km permitted the vertically pointing lidar ceilometer at Chilbolton to observe the lowest of the

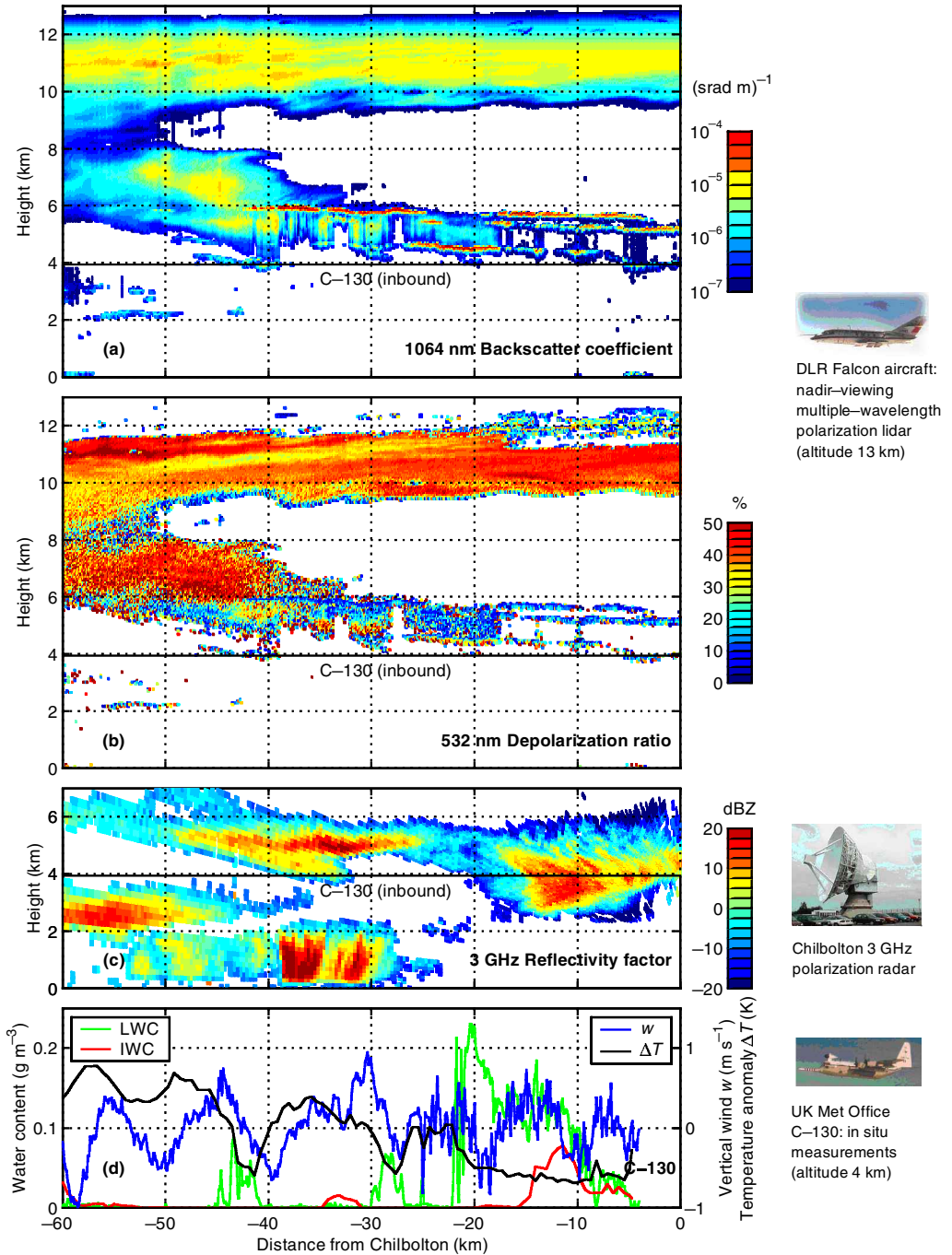


Figure 3. Composite of observations from the inbound run leading up to the 1420 UTC over-flight of Chilbolton on 20 October 1998 during CLARE'98 (see text). Panels (a) and (b) show measurements by the nadir-pointing ALEX lidar on board the Falcon aircraft flying at an altitude of 13 km. Simultaneous measurements of radar reflectivity  $Z$  by the ground-based 3 GHz radar at Chilbolton are shown in panel (c), and panel (d) shows liquid-water content (LWC), ice-water content (IWC), vertical wind ( $w$ ) and the temperature anomaly ( $\Delta T$ ) as measured by the C-130 aircraft at an altitude of 4 km.

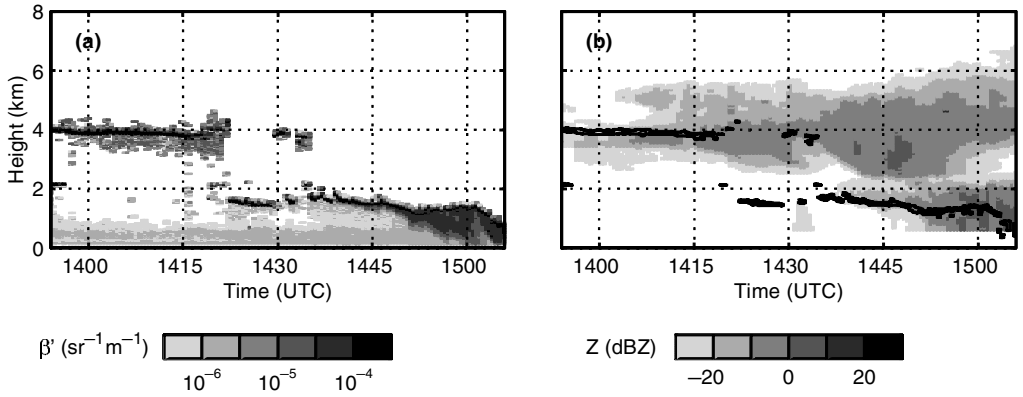


Figure 4. (a) Attenuated lidar backscatter coefficient ( $\beta'$ ) measured by the vertically pointing 905 nm lidar ceilometer and (b) reflectivity factor ( $Z$ ) from the 94 GHz Galileo radar, during the period of the aircraft overflights on 20 October 1998. The  $\beta' = 8 \times 10^{-5}$  ( $\text{sr m}^{-1}$ ) contour is overlaid on the reflectivity image.

supercooled layers at 4 km. This is shown in Fig. 4, together with the reflectivity measured by the Galileo radar. The layer persisted throughout the 25 min period and was too optically thick for any of the higher layers to be seen. The maximum values of  $\beta'$  measured by the ground-based lidar in the layer were around  $3.5 \times 10^{-4}$  ( $\text{sr m}^{-1}$ ). In section 5 the optical depth of the layers is calculated from the remote observations.

### (c) *In situ observations*

The Met Office C-130 aircraft was making *in situ* microphysical measurements at an altitude of 4 km, where the temperature was  $-7^\circ\text{C}$ , and where the ground-based lidar ceilometer indicated the presence of a liquid-water layer. The last panel of Fig. 3 shows its measurements of LWC, IWC, vertical wind and temperature anomaly (i.e. with the run-mean temperature of  $-7^\circ\text{C}$  subtracted). In the vertical-wind measurements, a wave with an amplitude of around  $0.6 \text{ m s}^{-1}$  and a wavelength of 15 km is clearly present, and beyond around 25 km from Chilbolton a wave with the same wavelength is also apparent in temperature, but offset by  $90^\circ$ . A maximum-entropy cross-spectral analysis of vertical wind and temperature provides clear evidence that the wave is a linear gravity wave, although its origin is unclear. The wave is most distinct beyond 26 km, and the isolated peaks in LWC (up to around  $0.05 \text{ g m}^{-3}$ ) centred at 28 and 43 km from Chilbolton are clearly associated with it as both coincide with minima in temperature, corresponding to the greatest vertical displacement. We estimate the peak vertical displacement to be around 80 m, which is consistent with the observed LWC at this temperature. The airborne-lidar signal was very weak at 4 km because of the strong attenuation by the layers above, but there is a suggestion of a highly reflective layer at the altitude of the C-130 that coincides with the *in situ* measurements of liquid water. The effective radius ( $r_e$ ) of the liquid-water droplets in these peaks was measured by the FSSP to be  $2 \mu\text{m}$ , which is smaller than in most liquid-water clouds and suggests that they had only been growing for a few minutes. It is possible that all the layers of supercooled water observed during this event originated in the ascent associated with gravity waves. When the aircraft penetrated the main body of the cloud at a range of around 22 km from Chilbolton, the vertical-wind trace shows much more turbulence, although the larger-scale wave is still apparent. Here, the LWC reached a peak value of  $0.2 \text{ g m}^{-3}$ , and the droplet  $r_e$  was a little higher at  $3\text{--}5 \mu\text{m}$ .

The rate of ice-particle growth by riming and vapour deposition was calculated from the particle size spectra measured during the aircraft run shown in Fig. 3, using the formulae in Pruppacher and Klett (1997). It was found that, even in the region of maximum liquid-water content 20 km from Chilbolton, ice growth by vapour deposition was at least a factor of two larger than that by riming. The maximum ice growth rate for the run was around  $0.2 \text{ g m}^{-3} \text{ h}^{-1}$ , and occurred in the region with the highest ice-water content, although only 15% of this growth was due to riming.

(d) *Differential-reflectivity observations*

We next describe differential-reflectivity ( $Z_{\text{DR}}$ ) measurements made by CAMRa at the same time as the highly reflective layers were measured by the airborne lidar.  $Z_{\text{DR}}$  is defined as the ratio of reflectivities measured at horizontal (H) and vertical (V) polarizations, expressed in logarithmic units as

$$Z_{\text{DR}} = 10 \log_{10} \left( \frac{Z_{\text{H}}}{Z_{\text{V}}} \right) \text{ dB.} \quad (1)$$

Non-spherical particles falling with their largest axis in the horizontal scatter the horizontally polarized beam more strongly, resulting in positive  $Z_{\text{DR}}$ . It is known that ice crystals tend to fall with their major axis in the horizontal (Cho *et al.* 1981; Pruppacher and Klett 1997). The magnitude of  $Z_{\text{DR}}$  is determined by the axial ratio, density and fall mode of the targets. In ice clouds  $Z_{\text{DR}}$  usually lies in the range 0–0.5 dB, indicating the presence of bullet rosettes, side planes or low-density aggregates. High values in stratiform ice clouds can occur only when the radar signal is dominated by the contribution from solid ice crystals with extreme axial ratios, i.e. columns, plates or dendrites.

Figure 5 shows lidar  $\beta'$  and radar  $Z_{\text{DR}}$  for the run shown in Fig. 3 (panels (e) and (f) of Fig. 5), together with two of the previous runs and the run immediately afterwards. Unfortunately the C-130 was only available for the last two of these runs. In the first three runs depicted in Fig. 5, the presence of liquid-water layers (visible to the lidar) seems to be associated with extremely high  $Z_{\text{DR}}$ , particularly beneath the layer at cloud top where values up to 7 dB were attained. We can interpret this as due to the rapid depositional growth of pristine plates or dendrites in the highly supersaturated environment. Lower in the cloud the particles became large enough to aggregate, which had the effect of both reducing the effective particle density and making them more spherical, and  $Z_{\text{DR}}$  fell back to its more usual range of 0–0.5 dB. Similarly high values of  $Z_{\text{DR}}$  were observed by Hall *et al.* (1984) at the top of stratiform ice clouds, although without any simultaneous measurements of liquid water or the suggestion that the presence of liquid water could be important.

In Figs. 5(c) and (e), ice is observed to fall into the west-most (left-most) liquid-water layer from above, which has the immediate effect of reducing  $Z_{\text{DR}}$  beneath this layer. This is presumably because the ice particles from above had already aggregated, and they then grew rapidly by deposition or riming on entering the liquid-water layer. By the last run the liquid water was completely depleted, and there is little sign of either highly reflective layers or ice crystals with extreme axial ratios. Indeed, the C-130 aircraft sampled at an altitude of 5.5 km ( $-15^\circ\text{C}$ ) during this run but no significant liquid water was detected.

Although the C-130 did not fly directly through the high- $Z_{\text{DR}}$  region, the values at the 4 km altitude of the aircraft during the run leading up to the 1420 UTC over-flight were still above average at a range of around 15 km from Chilbolton, and the crystals

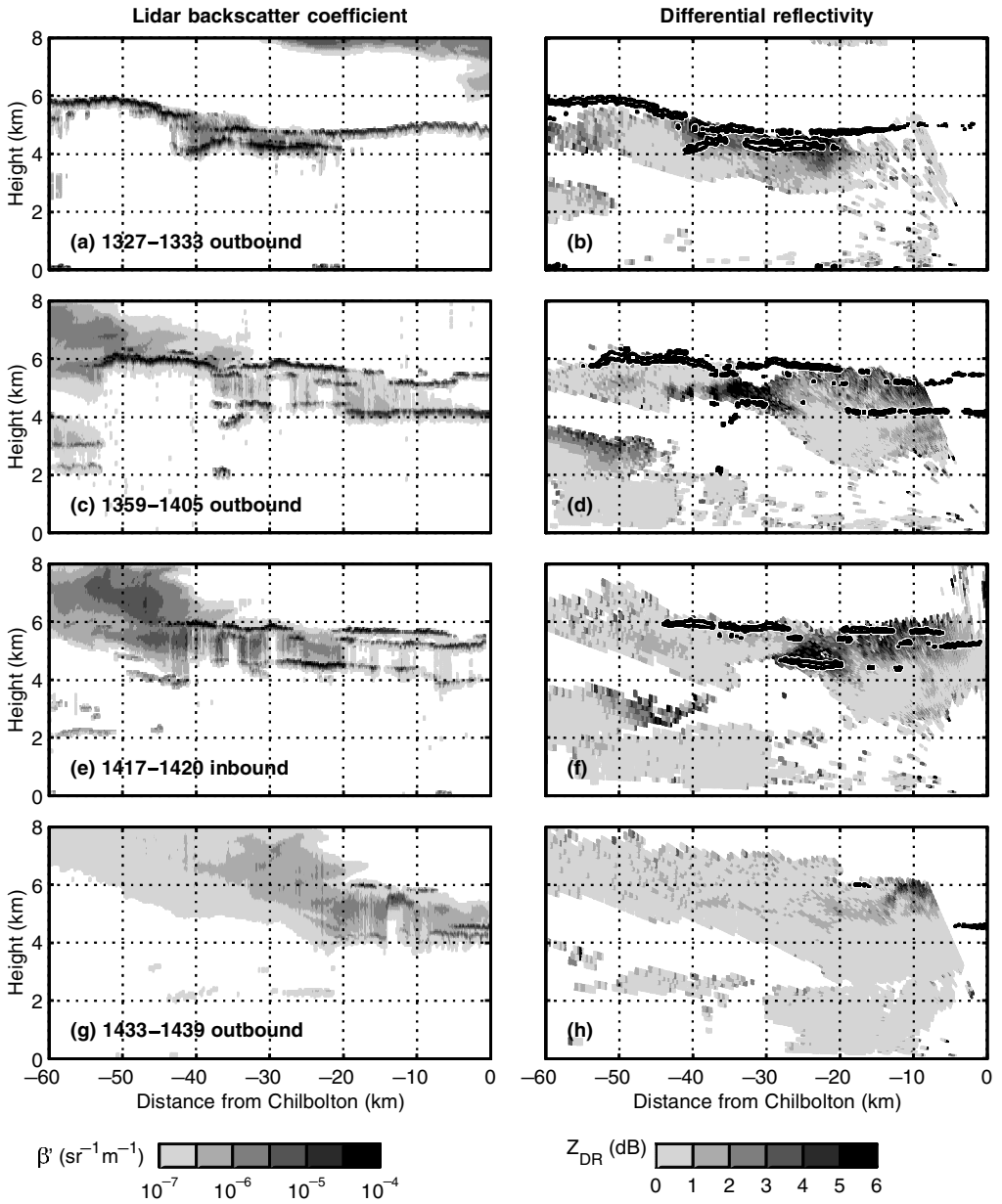


Figure 5. Simultaneous measurements of attenuated lidar backscatter coefficient  $\beta'$  from ALEX and radar differential reflectivity  $Z_{DR}$  from CAMRa, during four runs between 1327 UTC and 1439 UTC. The third run is the same as shown in Fig. 3. The  $\beta' = 1.25 \times 10^{-5} \text{ (sr m)}^{-1}$  contour is overlaid on the  $Z_{DR}$  image. The C-130 was only present in the last two of these runs.



Figure 6. Crystal images from the two-dimensional (2D) cloud probe (a) and 2D precipitation probe (b) beneath the high- $Z_{DR}$  region that was shown in Fig. 5(f), 15 km from Chilbolton at an altitude of 4 km. The array width of the 2D cloud probe is  $800 \mu\text{m}$  and that of the 2D precipitation probe is  $6400 \mu\text{m}$ .

sampled will have been strongly affected by the liquid-water layers above. Figure 6 shows 1 mm crystals measured by the 2D-C and 2D-P at around this location, where  $Z_{DR}$  was around 1 dB; it would have taken around 15 min for crystals to grow to this size by vapour diffusion at  $-10^\circ\text{C}$ . The crystals in the 2D-C images exhibit the distinctive broad branches characteristic of sector plates, known to grow only at temperatures of less than  $-9^\circ\text{C}$  and at supersaturation with respect to liquid water (e.g. Young 1993). Assuming the density of sector plates to be  $0.5 \text{ g cm}^{-3}$  (Young 1993) and the crystals to be horizontally aligned, the maximum measured  $Z_{DR}$  of 4.5 dB in Fig. 5(f) corresponds to an axial ratio in excess of 10:1 (Hogan *et al.* 2002). This ratio is comparable with the values obtained from the appropriate diameter–width relationships of Ono (1970) using a diameter of 1 mm, but is very difficult to verify from the 2D images because the plates would have to be aligned perfectly for the axial ratio to be discerned, and generally local flow distortion as crystals enter the 2D probes makes their orientation random (Gayet *et al.* 1993).

#### 4. 21 OCTOBER 1998 CASE-STUDY

The cold front that had been over the Atlantic on 20 October 1998 cleared Chilbolton by 0900 UTC the following day and was followed by a strong south-westerly airflow with a moist layer between 350 hPa and 500 hPa (Figs. 7 and 8). In four runs between 1000 and 1050 UTC the nadir-viewing ALEX lidar on board the Falcon aircraft at an altitude of 10 km observed glaciating altocumulus between 4.5 km and 6.5 km. As on 20 October, a highly reflective layer was present at the top of the cloud. In fact, the strength of the echo from this layer was such that the receiver of the ALEX lidar saturated, rendering both the backscatter coefficient and depolarization ratio from this instrument highly unreliable, so they are not used in this section. For one run only, between 1025 and 1037 UTC, the ARAT aircraft at an altitude of between 3.0 and 3.9 km turned its Leandre lidar to zenith. The observations of this case are, therefore, rather less comprehensive than on 20 October, but they provide a valuable contrasting case for the radiation calculations in section 5. According to the Unified Model, the wind during this run was  $28 \text{ m s}^{-1}/251^\circ$  at the altitude of the C-130,  $9^\circ$  from the  $260^\circ$  azimuth along which the three aircraft were flying. As in section 3(a), the measurements from each instrument were displaced using the component of the wind along this azimuth such that each should represent a ‘snap shot’ of the clouds at the instant that the 3 GHz radar began scanning down from zenith.

The Leandre measurements of backscatter coefficient and depolarization ratio are depicted in Figs. 9(a) and (b). The highly reflective layer at cloud top coincided with the

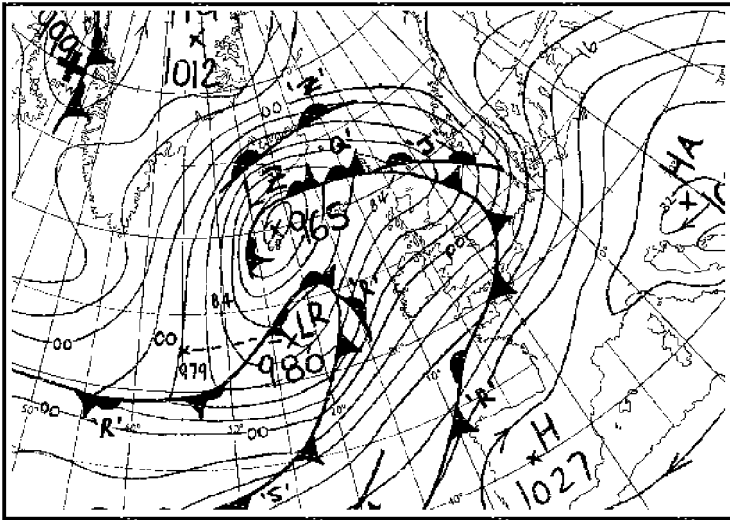


Figure 7. UK Met Office surface analysis at 12 UTC on 21 October 1998.

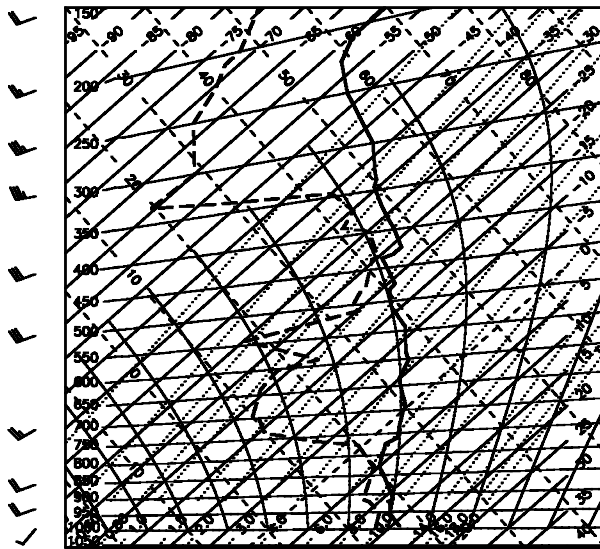


Figure 8. Tephigram of the Larkhill radiosonde ascent at 1000 UTC on 21 October 1998.

water-saturated layer at 430 hPa in the radiosonde ascent (Fig. 8) and, as on 20 October 1998, had a low depolarization, further evidence that the layer was composed of liquid water. The layer was significantly more optically thick than on the day before, and multiple scattering appears to have caused fairly rapid depolarization of the beam as it penetrated further into the layer. Note that the molecular return is much more evident in Fig. 9(a) than in Fig. 3(a) because of the 16-fold increase in the efficiency of Rayleigh scattering at 532 nm compared with 1064 nm.

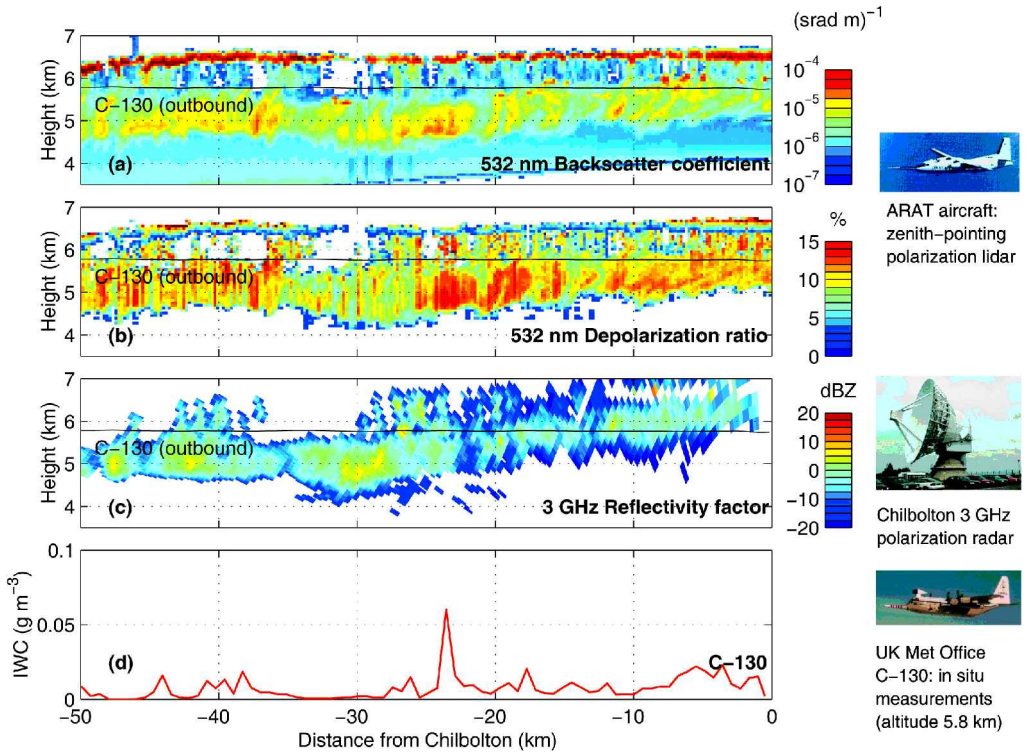


Figure 9. Composite of observations from the 1025–1037 UTC run on 21 October 1998. Panels (a) and (b) show measurements by the Leandre lidar in zenith-pointing configuration on board the ARAT aircraft. Simultaneous measurements of radar reflectivity  $Z$  by the ground-based 3 GHz radar at Chilbolton are shown in panel (c), and panel (d) shows ice-water content measured by the C-130 aircraft at an altitude of 5.8 km. The altitude of the ARAT varied by 900 m during the run, explaining the variation in the height of the first lidar pixel in each ray of panel (a).

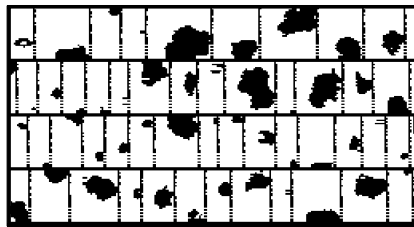


Figure 10. Typical ice-particle images from the two-dimensional cloud probe on board the C-130 as it flew through the cloud shown in Fig. 9, at an altitude of 5.8 km. The array width of the probe is  $800 \mu\text{m}$ .

The corresponding 3 GHz radar measurements are shown in Fig. 9(c), and it can be seen that the radar was only able to detect the ice-particle fall streaks beneath the layer, but not the layer itself. Figure 9(d) shows the fairly low ice-water contents that were measured by the C-130 aircraft at 5.8 km in the fall streaks. No significant liquid water was measured at this altitude. Figure 10 shows typical images from the 2D cloud probe; the ice crystals appear to be quasi-spherical and between  $150$  and  $600 \mu\text{m}$  in size.

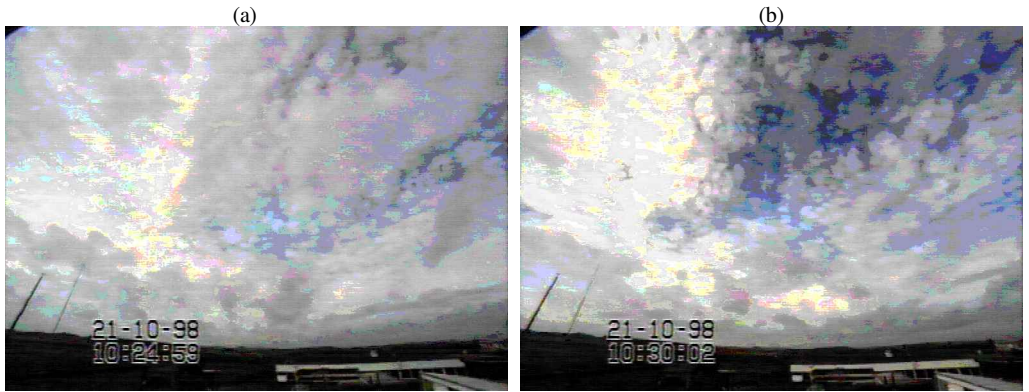


Figure 11. Photographs of the sky over Chilbolton at (a) 1025 UTC on 21 October 1998, when the C-130 passed overhead at the start of its outbound leg and the 3 GHz radar began scanning, and at (b) 1030 UTC. The view is approximately along the aircraft flight track and the opening angle of the lens is  $88^\circ$  in the vertical and  $107^\circ$  in the horizontal.

Photographs of the sky taken at the start of the run and 5 min later are shown in Fig. 11, and demonstrate the cellular nature of the liquid-water layer. Some intermittent low-level cloud was also present. Although some gaps in the supercooled cloud are evident in both the photographs and the lidar data, the cloud itself was generally too thick for its optical depth to be estimated using lidar; it attenuated the lidar signals so strongly that neither the molecular nor (in the case of the ALEX lidar) the ground returns beyond it were detectable. However, the albedo measured by the Falcon during this run was between 0.4 and 0.6, and this information was used by Francis *et al.* (1999) to estimate optical depth. When they assumed that the layer was composed of liquid water then the resulting visible optical depth ranged between 3 and 8. If they assumed it to be composed of ice then the required optical depth was much higher.

##### 5. DETERMINATION OF THE RADIATIVE EFFECT OF LAYERS OF SUPERCOOLED WATER

We now estimate the effect of the supercooled water layers on the radiation field by retrieving three profiles of extinction coefficient and effective radius from the remote observations, and using them as input to a radiative-transfer model. Radiation calculations are performed both with and without the supercooled water. Profiles of ice-cloud properties are obtained by combining backscatter measurements at two different frequencies and utilizing the different size dependence of the backscattering efficiency to derive particle size. The radar/lidar method was first used by Intrieri *et al.* (1993) and has the potential to be accurate because of the much stronger dependence of radar reflectivity factor on size compared with lidar backscatter coefficient. However, correction must first be made for attenuation of the lidar signal. When lidar attenuation is too strong, such as in the presence of supercooled liquid-water clouds, we make use of 35 GHz and 94 GHz radars; the larger ice particles scatter outside the Rayleigh regime at the higher frequency and the ratio of reflectivity at the two wavelengths can be related to particle size (Sekelsky *et al.* 1999; Hogan *et al.* 2000).

It should be noted that the principal objective in this section is to get an idea of the typical radiative effect that supercooled liquid water could have in realistic mixed-phase clouds, not to rigorously evaluate the lidar–radar and dual-wavelength radar methods for retrieving ice-particle properties. Hence, moderate errors in the retrievals are tolerable for these purposes.

## (a) Retrieval technique

We assume that the ice-particle size distribution  $n(D)$  may be described by a gamma distribution:

$$n(D) = N_0 D^\mu \exp\{-(3.67 + \mu)D/D_0\}, \quad (2)$$

where  $D$  is the equivalent-area diameter (i.e. the diameter of a sphere with the same cross-sectional area as the actual particle),  $D_0$  is the median volume diameter, and  $\mu$  is the ‘shape parameter’ of the distribution.  $N_0$  is a concentration scaling parameter and is eliminated when the ratio of backscatter at two different frequencies is calculated.

Ice particles are assumed to scatter according to geometric optics at lidar wavelengths, with the result that the visible extinction coefficient,  $\alpha$ , is proportional to twice the cross-sectional area:

$$\alpha = \frac{\pi}{2} \int_0^\infty n(D) D^2 dD, \quad (3)$$

while at radar frequency  $f$  we assume that the ice particles may be approximated as homogeneous spheres with the same mass and cross-sectional area, and radar reflectivity is then given by:

$$Z_f = |K_i|^2 \int_0^\infty n(D) \left(\frac{\rho}{\rho_i}\right)^2 D^6 \gamma_f(D) dD, \quad (4)$$

where  $|K_i|^2$  is the ‘dielectric factor’ of solid ice (essentially constant at 0.174 for frequencies between 0.1 and 1000 GHz),  $\gamma_f(D)$  is the Mie/Rayleigh backscattering ratio,  $\rho$  is the effective density of the ice–air mixture and  $\rho_i$  is the density of solid ice. We have applied Debye’s solution (Battan 1973), in which radar reflectivity is proportional to the square of the effective density. Francis *et al.* (1998) derived the following relationship between mass  $m$  and cross-sectional area  $A$  from a large aircraft dataset (although they expressed their relationship in terms of melted-equivalent diameter):

$$\begin{aligned} m &= 0.691A^{1.5} \text{ mg}; & A \leq 0.0052 \text{ mm}^2 \\ m &= 0.122A^{1.17} \text{ mg}; & A > 0.0052 \text{ mm}^2, \end{aligned} \quad (5)$$

with  $A$  measured in  $\text{mm}^2$ . From this the following expression for density as a function of equivalent-area diameter (mm) may be derived (Hogan *et al.* 2000):

$$\begin{aligned} \rho &= 0.917 \text{ g m}^{-3}; & D \leq 0.081 \text{ mm} \\ \rho &= 0.175D^{-0.66} \text{ g m}^{-3}; & D > 0.081 \text{ mm}. \end{aligned} \quad (6)$$

The impact of uncertainties in density on the retrievals is discussed below. It should be noted that the use of integrals from 0 to infinity in Eqs. (3) and (4) is not expected to introduce significant error, since for a first-order gamma distribution with a median volume diameter of 1 mm, 90% of the extinction is attributable to particles of diameter less than 1.4 mm and 90% of the radar reflectivity factor (in the Rayleigh scattering approximation) is attributable to particles smaller than 2.5 mm.

Effective radius was defined for ice clouds by Foot (1988) as

$$r_e = \frac{3 \text{ IWC}}{2 \rho_i \alpha}, \quad (7)$$

and similarly for liquid-water clouds. Thus, by considering size distributions with a range of values for  $D_0$ , we can simulate the relationship between  $r_e$ , radar–lidar ratio

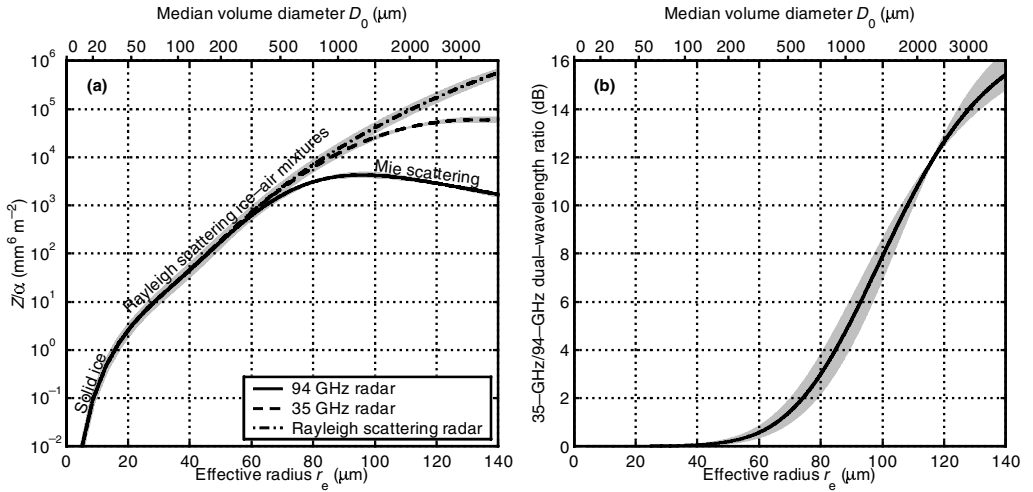


Figure 12. Variation of (a) radar–lidar ratio ( $z/\alpha$ ) and (b) dual-wavelength radar ratio, with effective radius. The black lines indicate the results for shape parameter  $\mu$  of 1 in Eq. (2), while the grey bands indicate the range of retrievals associated with  $\mu$  varying between 0 and 3.

and dual-wavelength radar ratio. The results are depicted in Fig. 12, for an assumed shape parameter  $\mu$  of 1. For  $r_e$  up to around  $60 \mu\text{m}$ , the radar–lidar method is potentially the most sensitive, with a  $20 \mu\text{m}$  change in  $r_e$  corresponding to at least an order of magnitude change in the radar–lidar ratio. However, when  $r_e > 80 \mu\text{m}$  (which is equivalent to  $D_0 > 800 \mu\text{m}$ ), then Mie scattering acts to reduce the measured radar reflectivity factor at 94 GHz such that it has a similar size dependence to the lidar, with the result that the radar–lidar ratio is almost constant and no size information can be inferred. The same problem occurs at 35 GHz when  $r_e > 120 \mu\text{m}$ . For  $r_e > 60 \mu\text{m}$ , however, the ratio of reflectivities at 35 GHz and 94 GHz contains useful size information and has the advantage that it can be used when liquid water is present that would strongly attenuate the lidar signal. The grey bands in Fig. 12 indicate the effect of using  $\mu$  values ranging between 0 and 3; it can be seen that this changes retrieved  $r_e$  from the  $\mu = 1$  line by only  $2.5 \mu\text{m}$  in the case of the radar–lidar technique and at most  $4 \mu\text{m}$  for the dual-wavelength radar technique. Kosarev and Mazin (1989) found typical values of  $\mu$  between 0 and 1, although their dimension was based on the maximum physical extent of the particle, rather than the equivalent-area diameter.

Hogan *et al.* (2000) showed that although the dual-wavelength radar technique is fairly insensitive to  $\mu$ , axial ratio and ice density can potentially be quite important. In the case of axial ratio, we use 3 GHz  $Z_{\text{DR}}$  to indicate where the assumption of sphericity is significantly in error, and apply the technique only in regions where  $Z_{\text{DR}}$  is close to 0 dB. Density would, therefore, seem to be the main uncertainty in the retrieval. Hogan *et al.* (2000) found that the effect on dual-wavelength radar retrievals of using the  $\rho = 0.07D^{-1.1} \text{ g m}^{-3}$  relationship of Brown and Francis (1995) instead of the form shown in Eq. (6) was a 20% change in the retrieved  $D_0$  and a factor-of-two change in retrieved IWC. It is likely that similar uncertainties are present for IWC and size retrieved using the radar–lidar technique.

### (b) Profile 1

The first vertical profile is shown in Fig. 13 and corresponds to the end of the 1417–1420 UTC inbound run on 20 October 1998 shown in Fig. 3. The Falcon aircraft passed

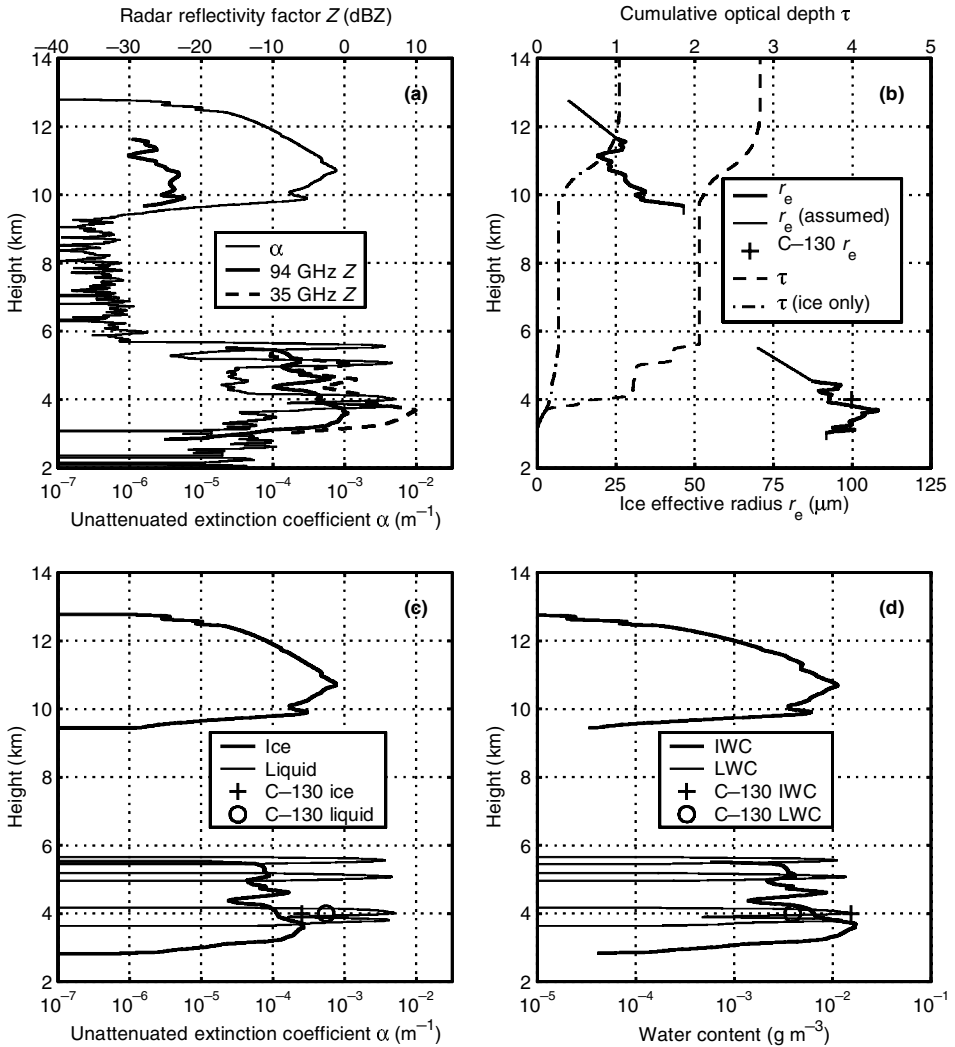


Figure 13. Retrieval of ice- and liquid-cloud properties from lidar and dual-wavelength radar for 'profile 1', at around 1420 UTC on 20 October 1998: (a) attenuation-corrected extinction profiles from the ALEX lidar and effective radar reflectivity factor from the 35 GHz and 94 GHz radars; (b) ice effective radius derived from the radar and lidar profiles, and cumulative visible optical depth of the ice cloud only and of all cloud; (c) extinction coefficient of the ice- and liquid-water phases; (d) liquid-water content (LWC) and ice-water content (IWC), assuming a liquid effective radius of  $4.5 \mu\text{m}$ . The retrieval process is described fully in the text.

over Chilbolton at 1421 UTC, and the corresponding unattenuated  $\alpha$  profile is shown by the thin line in Fig. 13(a). Attenuation correction was performed using the 355 nm and 532 nm molecular returns at the far side of the cloud to provide a total optical-depth constraint, which was then partitioned with height assuming a constant extinction-to-backscatter ratio, or 'lidar ratio' (Klett 1985). The value for the lidar ratio was found to be 15 sr, close to the theoretical value for liquid-water droplets. Using lidar ratios of 14 and 17 sr in the inversion changes the retrieved total optical depth by  $-22\%$  and  $+36\%$ , respectively.

Four highly reflective layers, which we assume to be liquid water, were present between 3.8 km and 5.6 km, while cirrus was observed between 9 km and 13 km. The  $r_e$  of the cirrus was first estimated by combining the lidar  $\alpha$  measurements with the reflectivity factor of the 94 GHz Miracle (the thick solid line above 9 km in Fig. 13(a)); the result is shown by the thick line in Fig. 13(b), ranging from 20 to 45  $\mu\text{m}$ . The radar did not detect the full extent of the cloud so, for the purposes of the radiation calculations in the next section, we arbitrarily assume a cloud-top  $r_e$  of 10  $\mu\text{m}$  which increases linearly down to the first radar measurement. At the base of the cirrus,  $r_e$  is assumed to be constant in the 220 m where the lidar detected the cloud and the radar did not.

The ice properties of the midlevel cloud were estimated by dual-wavelength radar at the time the Falcon aircraft passed overhead. Lidar was not used for this purpose because of possible errors due to uncertain attenuation by the liquid-water layers, and the fact that small amounts of liquid water could still be present between the layers. The thick solid and dashed lines below 6 km in Fig. 13(a) show the 94 GHz Galileo and 35 GHz Rabelais radar measurements, respectively. Below 4.5 km the dual-wavelength ratio was large enough to estimate effective radius using the relationship plotted in Fig. 12(b), and the results are shown in Fig. 13(b), ranging from 85 to 110  $\mu\text{m}$ . We assume that the ice effective radius at the top of the midlevel cloud is 70  $\mu\text{m}$ , similar to the value obtained at this altitude from radar and lidar in the next profile (Fig. 14(b)). Then from  $Z$  and  $r_e$ , the ice extinction coefficient  $\alpha$  was calculated using the relationship plotted in Fig. 12(b). Ice-water content was calculated from  $r_e$  and  $\alpha$  using Eq. (7). Finally, the peaks in extinction coefficient measured by the ALEX lidar in the midlevel cloud were assumed to be entirely attributable to liquid water, and liquid-water content was calculated by assuming that the liquid-water effective radius was 4.5  $\mu\text{m}$  for all supercooled liquid-water clouds. This was a typical value measured by the C-130 FSSP in the thicker supercooled liquid-water clouds on 20 October 1998.

Figures 13(c) and (d) show the resulting ice and liquid extinction coefficients and water contents that are to be used in the radiation calculations. Figure 13(b) also shows the corresponding cumulative visible optical depth of the clouds with and without the contribution from liquid water. The optical depth of the midlevel cloud was around 2, although only around 0.25 of this was due to ice. The C-130 aircraft measurements taken as it flew over Chilbolton 1 min earlier at an altitude of 4 km are also plotted in panels (b)–(d). The C-130 measurements of IWC and ice extinction coefficient are around a factor of two larger than those inferred from radar, although  $r_e$  is only around 10% larger. At this altitude the C-130 appears to have been flying between the lower two layers, and the liquid-water measurements are consistent with those estimated from the lidar.

### (c) Profile 2

The second profile occurred 12 min after the first, when the Falcon commenced its outbound leg, and a similar approach was used to calculate the microphysical properties. By this time the visible optical depth of the cirrus had fallen from 0.8 to 0.3, while the liquid water in the midlevel cloud was now concentrated in a double-peaked layer between 4 and 4.5 km that had an optical depth of around 2. Figure 14 shows the information for the profile plotted as in Fig. 13. The Miracle radar was again used in the high cirrus. The nearest vertically pointing 35 GHz data were taken 9 min earlier (at 1424 UTC) when the C-130 passed overhead at the start of its outbound run and the 35 GHz Rabelais started scanning. Since the dual-wavelength radar method can be sensitive to differences in reflectivity due to mismatched beams, the 94 GHz profile nearest to the 35 GHz profile was chosen for retrievals in the midlevel cloud, and was

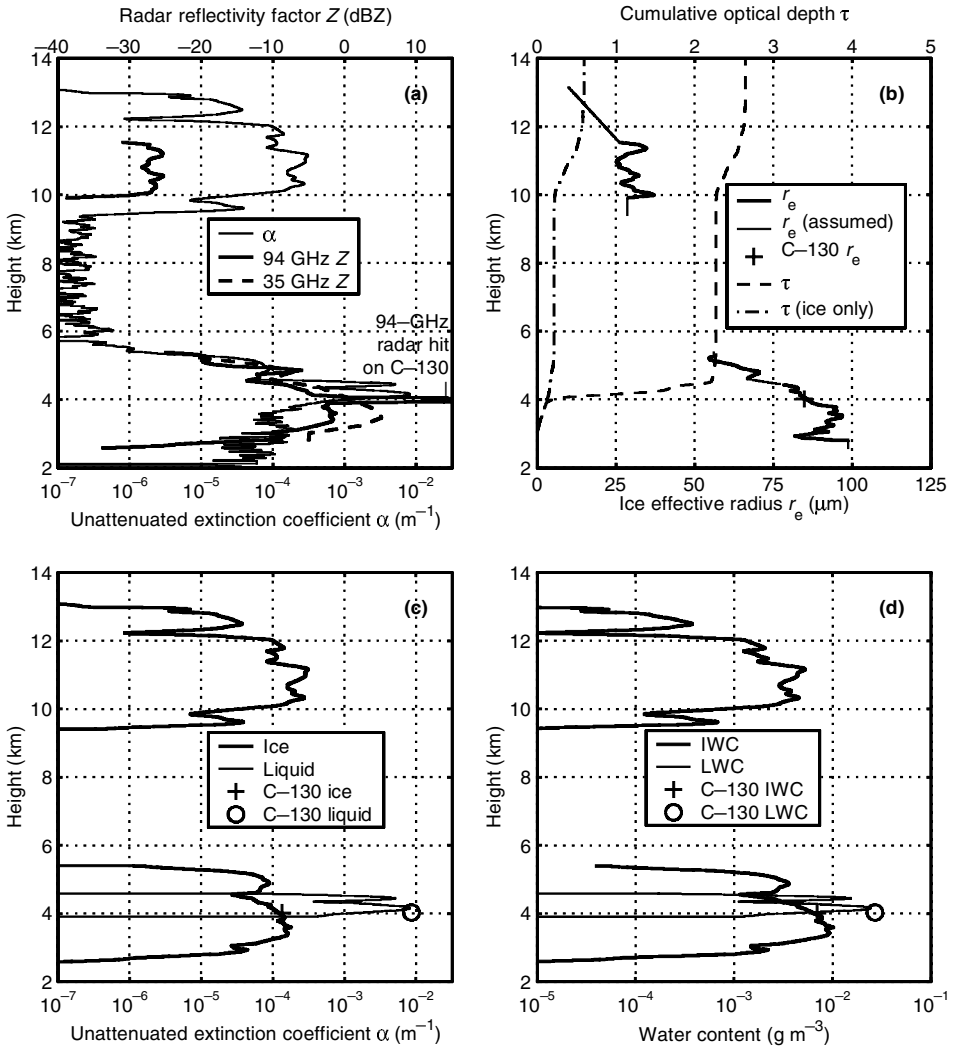


Figure 14. Retrieval of ice- and liquid-cloud properties from lidar and dual-wavelength radar for 'profile 2', at around 1430 UTC on 20 October 1998. The panels are the same as in Fig. 13.

from the Galileo radar. The C-130 was 'hit' by the Galileo in this profile, giving us confidence that *in situ* evaluation of the dual-wavelength retrieval can be performed at exactly the right location. Quante *et al.* (2000) also examined this event and compared the ALEX and Miracle profiles in the midlevel cloud at around 1433 UTC.

Above the liquid-water layer embedded in the midlevel cloud we use the lidar and 35 GHz radar data to estimate  $r_e$  and find it to range from 55 to 70  $\mu\text{m}$ . Below the liquid-water layer the dual-wavelength radar ratio indicates  $r_e$  ranging from 80 to 100  $\mu\text{m}$ . The C-130 ice measurements at the instant of the overhead pass are all in excellent agreement with the values inferred from radar (we interpolated across the strong peak in the Galileo signal corresponding to a hit on the aircraft). The C-130 liquid-water measurements were taken 8.3 km from Chilbolton, which assuming a radial wind speed of 18  $\text{m s}^{-1}$  (taken from the Unified Model) and no cloud evolution, should correspond

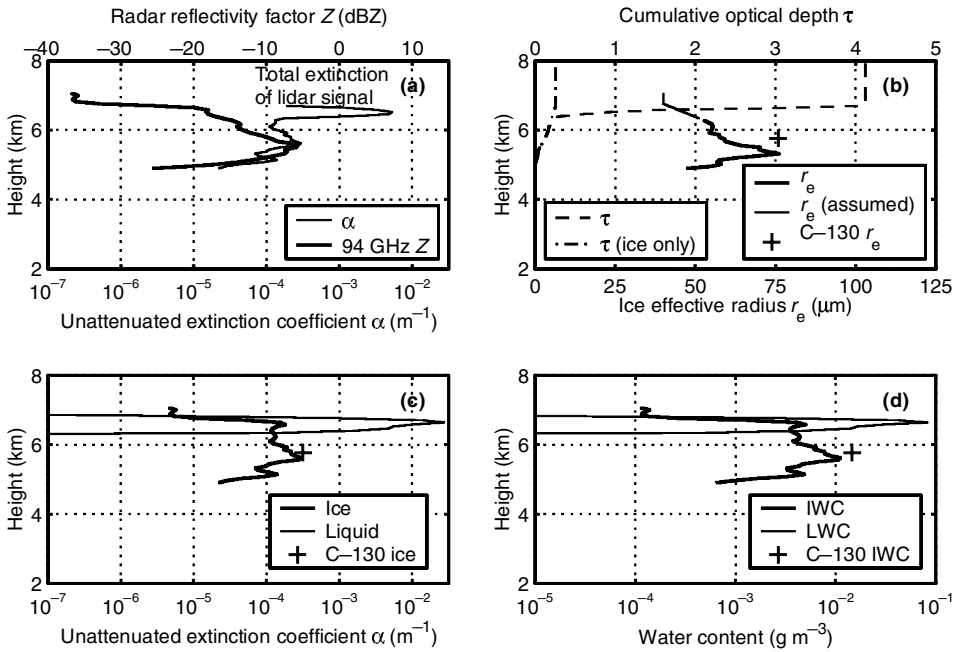


Figure 15. Retrieval of ice- and liquid-cloud properties from lidar and radar for ‘profile 3’, at around 1020 UTC on 21 October 1998: (a) attenuation-corrected extinction profiles from the Leandre lidar and effective radar reflectivity factor from the 95 GHz Miracle radar; (b) ice effective radius derived from the radar and lidar profiles, and cumulative visible optical depth of the ice cloud only and of all cloud; (c) extinction coefficient of the ice- and liquid-water phases; (d) liquid-water content (LWC) and ice-water content (IWC), assuming a liquid effective radius of 4.5  $\mu\text{m}$ .

to the lidar measurements at 1433 UTC. The aircraft measurements of liquid extinction coefficient and water content also agree well with the peak values inferred from lidar.

(d) Profile 3

The final profile was taken from the run shown in Fig. 9, on 21 October 1998. The Miracle radar profile at 1028 UTC is shown in Fig. 15(a), just after it switched from measuring Doppler spectra to its ordinary recording mode. As discussed in section 4, the ALEX lidar receiver saturated in this run, so we use data from the Leandre lidar. The ARAT commenced its outbound run 4 min earlier, so we have assumed a wind speed along the aircraft radial of 27  $\text{m s}^{-1}$  (from the Unified Model) and found the Leandre profile that would have passed over Chilbolton at the time the Miracle profile was taken; this is also shown in Fig. 15(a). An extinction-to-backscatter ratio in ice of 35 sr was assumed in order to make the slight correction for ice attenuation; the total optical depth of the ice was only around 0.25 (the value of 15 sr found for the profile in Fig. 13 was mostly due to liquid water). Below 6.2 km the lidar echo is assumed to be predominantly from ice, and  $r_e$  derived from the radar and lidar is shown by the thick line in Fig. 15(b). The highly reflective liquid-water layer above 6.2 km dominated the lidar signal so here we have arbitrarily assumed that the ice  $r_e$  dropped linearly to 40  $\mu\text{m}$  at the top of the layer. The C-130 *in situ* ice measurements are also depicted in Fig. 15 and show the values derived from radar and lidar to be somewhat underestimated;  $r_e$  is 20% lower,  $\alpha$  is 30% lower and IWC is around a factor of two too low.

The liquid-water layer above 6.2 km completely extinguished the lidar signal, making it impossible to estimate optical depth from the molecular return above the cloud. However, Francis *et al.* (1999) were able to estimate the optical depth of this layer using the passive radiation measurements on board the Falcon aircraft; the albedo of 0.45 implied an optical depth of around 4. The extinction coefficient of the liquid water, shown in Fig. 15(c), was increased to satisfy this finding.

(e) *Radiation calculations*

Radiative-transfer calculations using the Edwards and Slingo (1996) scheme were then performed on the three profiles to determine the radiative effect of the supercooled water. The long-wave calculations employed 300 spectral bands, with 220 bands being used in the short wave. A two-stream delta-Eddington solver was used for the calculations, requiring as input the extinction optical depth, single-scattering albedo  $\tilde{\omega}_0$ , and asymmetry parameter  $g$  for both water and ice clouds. These optical properties were calculated for the water clouds in terms of LWC and  $r_e$  using parametrizations of the form presented by Slingo and Schrecker (1982) in both the short wave and the long wave. The Mie calculations required to perform these parametrization fits were redone at a much higher spectral resolution than used in the original Slingo and Schrecker (1982) paper, in order to utilize the relatively large number of bands used in these comparisons. Hu and Stamnes (1993) have shown that the parametrization of water-cloud optical properties in terms of LWC and  $r_e$  in this manner yield extremely accurate results when compared with exact calculations.

The ice-cloud optical properties were calculated using the parametrization of Fu and Liou (1993), which assumes that the ice crystals are hexagonal columns. Although this crystal shape is probably not the most realistic when compared with the shapes observed in the *in situ* data, especially for the midlevel ice cloud (see Figs. 6 and 11), we used this parametrization because it treats the ice-cloud optical properties in a consistent manner across both the short-wave and long-wave spectral regions. In order to assess the likely errors associated with selecting an inappropriate crystal shape, we also carried out a parallel series of short-wave radiative-transfer calculations where either hexagonal plates, bullet-rosettes or planar polycrystals were assumed for the ice-crystal optical properties. These single-scattering calculations were carried out using the ray-tracing model described by Macke *et al.* (1996), and the results parametrized as functions of IWC and  $r_e$  in a similar manner to that described above. These parallel calculations showed that, when IWC,  $r_e$  and (most importantly) optical depth are constrained by the radar/lidar observations, the resulting short-wave fluxes differ by less than  $10 \text{ W m}^{-2}$ . The effects of changing crystal shape in the long wave will be even smaller than in the short wave, because ice absorption is so strong over much of the relevant thermal infrared region. These arguments suggest that the choice of crystal shape will not significantly affect any of our subsequent conclusions on the relative effects of ice and liquid.

The solar zenith angles used in the short-wave calculations were  $69.5^\circ$ ,  $70.5^\circ$  and  $64.9^\circ$  for profiles 1, 2 and 3 respectively. In accordance with the radar and lidar observations of this study, in layers where both ice and liquid water were present they were assumed to be mixed homogeneously for the purposes of calculating the layer single-scattering properties. In the first two profiles the vertical resolution of the calculations was variable; in the vicinity of the liquid-water layers it matched the 15 m resolution of the data, while elsewhere in the troposphere it varied between 50 m and 200 m. In the third profile the 60 m resolution of the data was used throughout the troposphere. We compare calculations performed with (a) clear skies, (b) only the ice

TABLE 1. WATER PATHS AND VISIBLE OPTICAL DEPTHS OF THE LIQUID AND ICE PHASES, FOR EACH OF THE THREE PROFILES DISCUSSED IN THE TEXT

Profile	Liquid-water path ( $\text{g m}^{-2}$ )	Ice-water path ( $\text{g m}^{-2}$ )	Liquid optical depth	Ice optical depth	Optical depth of ice above supercooled water
1	5.4	27.2	1.79	1.04	0.78
2	6.2	17.5	2.05	0.59	0.38
3	11.6	8.9	3.87	0.26	0.00

TABLE 2. TOP-OF-ATMOSPHERE RADIATION PARAMETERS FOR EACH OF THE THREE PROFILES DISCUSSED IN THE TEXT

Profile	Albedo	Outgoing long-wave radiation ( $\text{W m}^{-2}$ )	Reflected short-wave radiation ( $\text{W m}^{-2}$ )	Net absorbed radiation ( $\text{W m}^{-2}$ )	
1	Clear sky	0.13	245.0	61.5	175.8
	Ice only	0.30	179.4	145.4	157.6
	Liquid only	0.35	219.8	170.2	92.3
	All cloud	0.42	169.2	201.0	112.1
2	Clear sky	0.13	244.8	59.5	154.8
	Ice only	0.25	204.7	112.5	142.0
	Liquid only	0.37	221.3	171.4	66.4
	All cloud	0.41	190.8	186.9	81.5
3	Clear sky	0.12	251.4	70.2	262.5
	Ice only	0.16	240.5	91.2	252.5
	Liquid only	0.45	195.3	260.2	128.6
	All cloud	0.45	194.2	264.4	125.6

TABLE 3. EFFECTS ON TOP-OF-ATMOSPHERE RADIATION PARAMETERS OF ICE CLOUD ONLY, LIQUID-WATER CLOUD ONLY, AND BOTH ICE- AND LIQUID-WATER CLOUDS

Profile	Outgoing long-wave radiation ( $\text{W m}^{-2}$ )	Reflected short-wave radiation ( $\text{W m}^{-2}$ )	Net absorbed radiation ( $\text{W m}^{-2}$ )	
1	Effect of ice	-65.7	+83.9	-18.2
	Effect of liquid water	-25.2	+108.7	-83.5
	Effect of ice and liquid water	-75.8	+139.5	-63.7
2	Effect of ice	-40.2	+52.5	-12.8
	Effect of liquid water	-23.5	+111.8	-88.4
	Effect of ice and liquid water	-54.0	+127.4	-73.3
3	Effect of ice	-11.0	+21.0	-10.0
	Effect of liquid water	-56.1	+190.0	-133.9
	Effect of ice and liquid water	-57.3	+194.1	-136.9

phase present, (c) only the liquid phase present and (d) both the ice- and liquid-water phases present.

The liquid- and ice-water paths and visible optical depths of the three profiles are listed in Table 1; it can be seen that the relative amount of supercooled liquid water increases through profiles 1 to 3. The resulting upwelling and downwelling broad-band fluxes are plotted versus height in Fig. 16, and the corresponding heating-rate profiles, calculated from the divergences of these fluxes, are depicted in Fig. 17. Table 2 lists the values of albedo, outgoing long-wave radiation, reflected short-wave radiation and net absorbed radiation for each case. To see more easily the overall effect of the various scenarios on the radiation budget, Table 3 lists the changes in these parameters that occur when ice, liquid, and both ice and liquid are added to the clear-sky profiles.

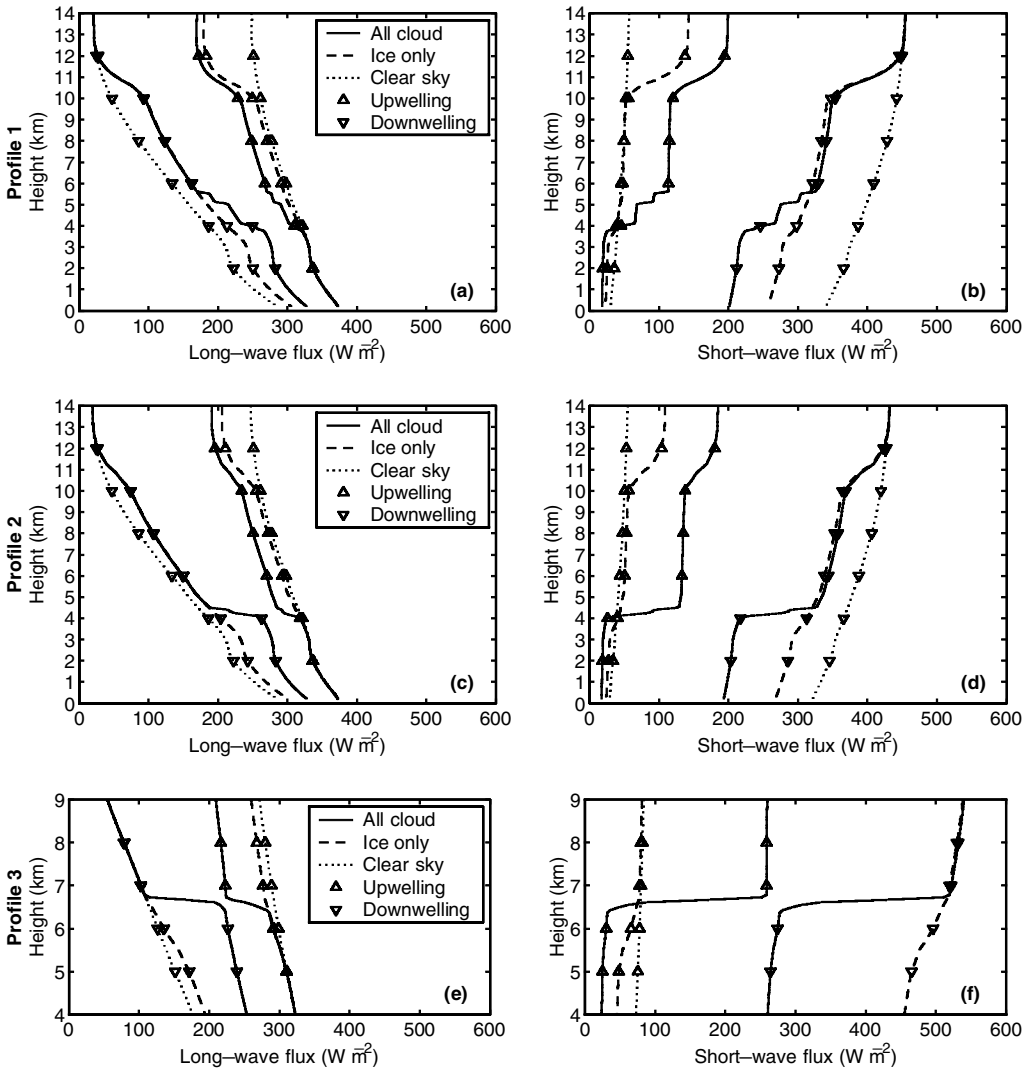


Figure 16. Upwelling and downwelling long-wave ((a), (c) and (e)) and short-wave ((b), (d) and (f)) fluxes calculated for the three profiles shown in Figs. 13–15. The different line styles correspond to calculations with both ice and liquid cloud present (solid lines), with only ice cloud present (dashed lines) and with no cloud present (dotted lines).

In profile 1 the liquid water was present in four individual layers, although the total liquid-water path (LWP) was only  $5.4 \text{ g m}^{-2}$ , five times less than the ice-water path (IWP). Comparing the ‘all cloud’, ‘ice only’ and ‘clear sky’ profiles in Fig. 16(a) we see that the liquid water dominated the radiative properties of the midlevel cloud in the long wave, where the ice had very little effect. This is indeed what would be expected from the much larger backscatter coefficients of the liquid-water layers compared with the ice in Fig 3. The peak cooling rate of the uppermost layer (due to long-wave emission to space) was around  $15 \text{ K day}^{-1}$  (Fig. 17(a)), although concentrated in a very thin layer. The outgoing long-wave radiation (OLR), however, was influenced most strongly by the

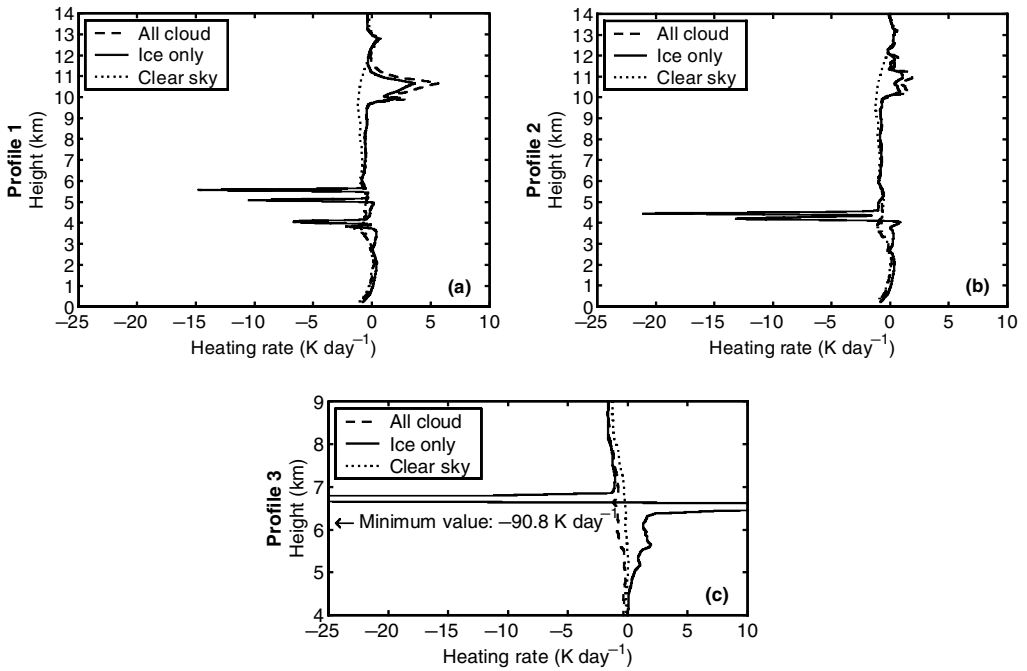


Figure 17. Heating-rate profiles calculated from the fluxes in Fig. 16.

cold, high cirrus, which had the effect of reducing OLR by  $65.7 \text{ W m}^{-2}$  from its clear-sky value (see Table 3). The liquid-water layers beneath caused an additional modest reduction of  $10.1 \text{ W m}^{-2}$  in this parameter.

The radiative effect of the liquid water in the short wave was much greater; the increase in reflected short-wave radiation due to liquid water alone was  $108.7 \text{ W m}^{-2}$  (compared with the clear-sky value), over four times greater than the corresponding decrease in OLR. Consequently, there was a quite substantial decrease in net absorbed radiation of  $83.5 \text{ W m}^{-2}$ . In contrast, the long-wave and short-wave effects of the ice cloud alone tended to cancel out (by virtue of the predominantly colder temperatures of the ice cloud), and the change in net absorbed radiation from the clear-sky value was only  $18.2 \text{ W m}^{-2}$ . With both ice and liquid water in the profile the decrease in net absorbed radiation was  $63.7 \text{ W m}^{-2}$ . Hence the high-level cirrus acted to partially offset the radiative effect of the liquid-water layers beneath.

The results for profile 2 are broadly similar to those for profile 1. A little more liquid water was concentrated in a double-peaked layer in a profile containing somewhat less ice, and consequently the relative importance of liquid water was greater. The effect of liquid water alone was to decrease the net absorbed radiation by  $88.4 \text{ W m}^{-2}$ , compared with a decrease of  $12.8 \text{ W m}^{-2}$  for ice alone.

The liquid water in profile 3 was concentrated in a single layer at  $-23 \text{ }^\circ\text{C}$ , with an LWP of  $11.6 \text{ g m}^{-2}$  and visible optical depth of nearly 4. The ice (with an IWP of  $8.9 \text{ g m}^{-2}$ ) was almost entirely beneath the liquid water, and consequently the liquid water dominated both the short-wave and long-wave properties of the cloud. The liquid water had the effect of decreasing OLR by  $56.1 \text{ W m}^{-2}$  while increasing the reflected short-wave radiation by  $190.0 \text{ W m}^{-2}$  (nearly a factor of four increase in albedo). The decrease in net absorbed radiation of  $133.9 \text{ W m}^{-2}$  was thus much larger than the

$10.0 \text{ W m}^{-2}$  decrease due purely to ice. Figure 17(c) shows that the peak cooling rate near the top of the liquid-water layer was  $90.8 \text{ K day}^{-1}$ , clearly large enough to drive convective overturning, explaining the cellular nature of the cloud shown in Fig. 11. This is similar to the value of around  $80 \text{ K day}^{-1}$  calculated by Heymsfield *et al.* (1991) for the top of  $-30^\circ\text{C}$  altocumulus cloud.

As for all clouds, the radiative effect of the supercooled liquid-water layers is of opposite sign in the long and the short wave, but, in these examples at least, the short-wave effect was three to five times stronger. Thus, by their increased reflection of solar radiation back to space, these clouds have an overall cooling effect in much the same way as stratocumulus. In each of these profiles the effect of liquid water on the net absorbed radiation was considerably more than the ice contribution, even when ice cloud was present above. However, the greatest cirrus optical depth considered was only 0.75 (in profile 1); presumably much thicker cirrus could significantly reduce the effect of the liquid water on the top-of-atmosphere radiation parameters.

## 6. CONCLUSIONS

In this paper we presented observations of supercooled liquid-water clouds between  $-7^\circ\text{C}$  and  $-23^\circ\text{C}$ . They occurred in the form of layers 100–200 m thick above or embedded within thicker ice clouds, and were easily identifiable from their very strong lidar return, while the radar return was dominated by the contribution from the larger ice particles. In the first case-study gravity waves were believed to be initially responsible for the vertical velocities that caused the condensation of liquid water, and *in situ* sampling at the crests of these waves found liquid-water contents of  $0.05 \text{ g m}^{-3}$  and effective radii of around  $2 \mu\text{m}$ . In both cases the optically thick liquid-water layers at cloud top then emitted strongly to space in the infrared, and the consequent cooling (Fig. 17) generated convective overturning sufficient to sustain the liquid water. The resulting cellular structure is evident on scales of around 500 m in Fig. 11. Ice falling beneath the uppermost layer presumably then depleted the ice nucleus concentration at that altitude enabling them to persist for longer periods. The available *in situ* data in the more mature supercooled clouds found liquid-water contents of  $0.1\text{--}0.2 \text{ g m}^{-3}$  and effective radii of  $3\text{--}5 \mu\text{m}$ .

Radiation calculations showed that, when present, supercooled liquid water can easily have a larger effect on the radiation field than the ice. Because supercooled-liquid clouds do not occur at temperatures colder than around  $-35^\circ\text{C}$ , their short-wave effect invariably outweighs the long-wave effect (by a factor of three to five in the cases discussed in section 5). Thus, they have a net cooling effect on climate, and in this way are rather similar to stratocumulus clouds (Heymsfield *et al.* 1991). The long- and short-wave effects of ice clouds at colder temperatures, on the other hand, tend to be more similar in magnitude.

There are several reasons why these layers are very unlikely to be represented realistically in current forecast and climate models. Firstly, many microphysics parametrizations have a minimum temperature below which liquid water cannot form (e.g.  $-9^\circ\text{C}$  for Moss and Johnson (1994),  $-15^\circ\text{C}$  for Smith (1990)). Secondly, the vertical resolution of current models in the midtroposphere is usually around 500 m, much thicker than the typical supercooled cloud thicknesses observed by lidar. Finally, the vertical velocities responsible for the formation and persistence of supercooled liquid seem to be very much associated with subgrid-scale phenomena such as cellular convection or gravity waves, rather than the large-scale ascent that might be represented by the grid-box-mean vertical velocity.

In order to evaluate the broader radiative importance of these clouds it is necessary to determine how often they occur. In the companion paper to this by Hogan *et al.* (2003), supercooled water clouds were identified in many months of data from a ground-based lidar at Chilbolton. It was found that 27% of clouds between  $-5^{\circ}\text{C}$  and  $-10^{\circ}\text{C}$  contained a highly reflective layer attributable to liquid water, falling to 6% of clouds between  $-25^{\circ}\text{C}$  and  $-30^{\circ}\text{C}$ . It was also shown that less than 30% of these layers had ice above them with a visible optical depth in excess of 0.5, so in most cases the supercooled liquid water will have dominated the radiative properties of the cloud.

To determine their full importance for climate, measurements are needed on a global scale. The proposed spaceborne cloud lidar and radar would be ideally suited to this task, as confirmed by Renger *et al.* (1995), who showed examples of highly reflective layers at temperatures as low as  $-35^{\circ}\text{C}$ , sampled simultaneously by the airborne ALEX lidar and the spaceborne lidar of the Lidar Inspace Technology Experiment. These could now be interpreted as being composed of supercooled liquid water. A spaceborne cloud radar alone, while having the capacity to make excellent measurements of ice-water content even in attenuating conditions for lidar (Liu and Illingworth 2000), may not be able to accurately constrain the radiation budget in some cases because of its inability to detect supercooled water.

#### ACKNOWLEDGEMENTS

We are indebted to the many people who were involved in CLARE'98, and would particularly like to thank the scientists and aircrew of the three research aircraft, the staff at Chilbolton, and Patrick Wursteisen of the ESA, for their hard work which ensured that the campaign was such a success. The Unified Model data were provided by Peter Panagi and Ed Dicks. The Galileo radar was developed for ESA by Officine Galileo, the Rutherford Appleton Laboratory and the University of Reading, under ESA Contract 10568/NL/NB. The CLARE'98 campaign was funded by ESA (grant 12957/98), and the analysis was also supported by the European Union through the 'Cloudnet' project (Grant EVK2-CT-2000-00065) and the Natural Environment Research Council (Grant GR3/00105).

#### REFERENCES

- |   |      |  |
|---|------|--|
| Battán, L. J.   | 1973 | <i>Radar observation of the atmosphere</i> . University of Chicago Press   |
| Bower, K. N., Moss, S. J.,<br>Johnson, D. W.,<br>Choullarton, T. W., Latham, J.,<br>Brown, P. R. A., Blyth, A. M.<br>and Cardwell, J. | 1996 | A parametrization of the ice water content observed in frontal and convective clouds. <i>Q. J. R. Meteorol. Soc.</i> , <b>122</b> , 1815–1844                    |
| Brown, P. R. A.   | 1993 | Measurement of the ice water content of cirrus using an evaporative technique. <i>J. Atmos. Oceanic Technol.</i> , <b>10</b> , 579–590                           |
| Brown, P. R. A. and Francis, P. N.  | 1995 | Improved measurements of the ice water content in cirrus using a total-water probe. <i>J. Atmos. Oceanic Technol.</i> , <b>12</b> , 410–414                      |
| Cho, H. R., Iribarne, J. V. and<br>Richards, W. G.  | 1981 | On the orientation of ice crystals in a cumulonimbus cloud. <i>J. Atmos. Sci.</i> , <b>38</b> , 1111–1115  |
| Eberhard, W. L.   | 1995 | Theory for dual-wavelength $\text{CO}_2$ lidar method to distinguish ice, mixed-phase, and water clouds. <i>J. Atmos. Oceanic Technol.</i> , <b>12</b> , 130–140 |
| Edwards, J. M. and Slingo, A.   | 1996 | Studies with a flexible new radiation code. 1: Choosing a configuration for a large-scale model. <i>Q. J. R. Meteorol. Soc.</i> , <b>122</b> , 689–719           |

- ESA (European Space Agency) 1999a 'CLARE'98 Cloud Lidar & Radar Experiment'. ESA Report WPP-170, ESTEC, Noordwijk, the Netherlands
- 1999b 'Earth Radiation Mission'. ESA Report SP-1233(3)—The four candidate Earth Explorer Core Missions, ESTEC, Noordwijk, the Netherlands
- Foot, J. S. 1988 Some observations of the optical properties of clouds. 2: Cirrus. *Q. J. R. Meteorol. Soc.*, **114**, 145–164
- Francis, P. N., Hignett, P. and Macke, A. 1998 The retrieval of cirrus cloud properties from aircraft multi-spectral reflectance measurements during EUCREX'93. *Q. J. R. Meteorol. Soc.*, **124**, 1273–1291
- Francis, P. N., Flentje, H., Pelon, J. and Testud, J. 1999 'An analysis of the airborne broad-band radiometer measurements collected during CLARE'98'. Pp. 225–229 in CLARE'98 Cloud Lidar And Radar Experiment, ESA Report WPP-170, ESTEC, Noordwijk, the Netherlands
- Fu, Q. and Liou, K. N. 1993 Parameterization of the radiative properties of cirrus clouds. *J. Atmos. Sci.*, **50**, 2008–2025
- Gardiner, B. A. and Hallett, J. 1985 Degradation of in-cloud forward scattering spectrometer probe measurements in the presence of ice particles. *J. Atmos. Sci.*, **2**, 171–180
- Gayet, J. F., Brown, P. R. A. and Albers, F. 1993 A comparison of in-cloud measurements obtained with 6 PMS 2D-C probes. *J. Atmos. Oceanic Technol.*, **10**, 180–194
- Goddard, J. W. F., Tan, J. and Thurai, M. 1994a Technique for calibration of meteorological radars using differential phase. *Electron. Lett.*, **30**, 166–167
- Goddard, J. W. F., Eastment, J. D. and Thurai, M. 1994b The Chilbolton Advanced Meteorological Radar: A tool for multi-disciplinary atmospheric research. *Electron and Commun. Eng. J.*, **6**, 77–86
- Gregory, D. and Morris, D. 1996 The sensitivity of climate simulations to the specification of mixed phase clouds. *Clim. Dyn.*, **12**, 641–651
- Hall, M. P. M., Goddard, J. W. F. and Cherry, S. M. 1984 Identification of hydrometeors and other targets by dual-polarization radar. *Radio Sci.*, **19**, 132–140
- Heymsfield, A. J., Miloshevich, L. M., Slingo, A., Sassen, K. and Starr, D. O'C. 1991 An observational and theoretical study of highly supercooled altocumulus. *J. Atmos. Sci.*, **48**, 923–945
- Hogan, R. J. and Goddard, J. W. F. 1999 'Calibration of the ground-based radars during CLARE'98'. Pp. 63–67 in CLARE'98 Cloud Lidar And Radar Experiment, ESA Report WPP-170, ESTEC, Noordwijk, the Netherlands
- Hogan, R. J. and Illingworth, A. J. 1999 The potential of spaceborne dual-wavelength radar to make global measurements of cirrus clouds. *J. Atmos. Oceanic Technol.*, **16**, 518–531
- Hogan, R. J., Illingworth, A. J. and Sauvageot, H. 2000 Measuring crystal size in cirrus using 35 and 94 GHz radars. *J. Atmos. Oceanic Technol.*, **17**, 27–37
- Hogan, R. J., Field, P. R., Illingworth, A. J., Cotton, R. J. and Choullarton, T. W. 2002 Properties of embedded convection in warm-frontal mixed-phase cloud from aircraft and polarimetric radar. *Q. J. R. Meteorol. Soc.*, **128**, 451–476
- Hogan, R. J., Illingworth, A. J., O'Connor, E. J. and Poiars Baptista, J. P. V. 2003 Characteristics of mixed-phase clouds. II: A climatology from ground-based lidar. *Q. J. R. Meteorol. Soc.*, **129**, 2117–2134
- Hu, Y. X. and Stamnes, K. 1993 An accurate parameterization of the radiative properties of water clouds suitable for use in climate models. *J. Climate*, **6**, 728–742
- Intrieri, J. M., Stephens, G. L., Eberhart, W. L. and Uttal, T. 1993 A method for determining cirrus cloud particle sizes using lidar and radar backscatter techniques. *J. Appl. Meteorol.*, **32**, 1074–1082
- Klett, J. D. 1985 Lidar inversion with variable backscatter/extinction ratios. *J. Atmos. Opt.*, **24**, 1638–1643
- Knollenberg, R. G. 1970 The optical array: An alternative to scattering for airborne particle size determination. *J. Appl. Meteorol.*, **9**, 86–103
- Kosarev, A. L. and Mazin, I. P. 1989 Empirical model of physical structure of the upper level clouds of the middle latitudes. Pp. 29–52 in *Radiation properties of cirrus clouds*. Nauka, Moscow
- Li, Z.-X. and Le Treut, H. 1992 Cloud-radiation feedbacks in a general circulation model and their dependence on cloud modelling assumptions. *Clim. Dyn.*, **7**, 133–139
- Liebe, H. J. 1985 An updated model for millimeter-wave propagation in moist air. *Radio Sci.*, **20**, 1069–1089

- Liu, C.-L. and Illingworth, A. J. 2000 Towards more accurate retrievals of ice water content from radar measurements of clouds. *J. Appl. Meteorol.*, **39**, 1130–1146
- Macke, A., Mueller, J. and Raschke, E. 1996 Single scattering properties of atmospheric ice crystals. *J. Atmos. Sci.*, **53**, 2813–2825
- Mörl, P., Reinhardt, M. E., Renger, W. and Schellhase, R. 1981 The use of the airborne lidar system 'ALEX F1' for aerosol tracing in the lower troposphere. *Contrib. Atmos. Phys.*, **54**, 401–410
- Moss, S. J. and Johnson, D. W. 1994 Aircraft measurements to validate and improve numerical model parametrizations of ice to water ratios in clouds. *Atmos. Res.*, **34**, 1–25
- Ono, A. 1970 Growth mode of ice crystals in natural clouds. *J. Atmos. Sci.*, **27**, 649–658
- Pelon, J., Flamant, P. H. and Meissonnier, M. 1990 'The French airborne backscatter lidar LEANDRE. 1: Conception and operation'. Pp. 36–39 in proceedings of the 15th international laser radar conference, 23–27 July 1990, Tomsk
- Pruppacher, H. R. and Klett, J. D. 1997 *Microphysics of clouds and precipitation. 2nd Ed.* Kluwer Academic Publishers
- Quante, M., Danne, O., Lemke, H., Milferstädt, D. and Raschke, E. 1998 'The GKSS 94 GHz cloud radar: System description and potential contributions in support of the Earth Radiation Mission'. Pp. 75–80 in ESA Report EWP-1968, ESTEC, Noordwijk, the Netherlands
- Quante, M., Lemke, H., Flentje, H., Francis, P. N. and Pelon, J. 2000 Boundaries and internal structure of mixed phase clouds as deduced from ground-based 95 GHz radar and airborne lidar measurements. *Phys. Chem. Earth*, **25**, 889–895
- Renger, W., Kiemle, C., Schreiber, H.-G., Wirth, M. and Moerl, P. 1995 'Airborne backscatter LIDAR measurements at 3 wavelengths during ELITE. ELITE-94, The European 'LITE' Correlative Measurement Campaign'. Pp. 15–35 in ESA Report WPP-107, ESTEC, Noordwijk, the Netherlands
- Sassen, K. 1984 Deep orographic cloud structure and composition derived from comprehensive remote sensing measurements. *J. Clim. Appl. Meteorol.*, **23**, 568–583
- 1991 The polarization lidar technique for cloud research—a review and current assessment. *Bull. Am. Meteorol. Soc.*, **72**, 1848–1866
- Sassen, K., Grund, C. J., Spinhirne, J. D., Hardesty, M. M. and Alvarez, J. M. 1990 The 27–28 October 1986 FIRE IFO case study: A five lidar overview of cloud structure and evolution. *Mon. Weather Rev.*, **118**, 2288–2311
- Sekelsky, S. M., Ecklund, W. L., Firda, J. M., Gage, K. S. and McIntosh, R. E. 1999 Particle size estimation in ice-phase clouds using multifrequency radar reflectivity measurements at 95, 33 and 2.8 GHz. *J. Appl. Meteorol.*, **38**, 5–28
- Slingo, A. and Schrecker, H. M. 1982 On the shortwave radiative properties of stratiform water clouds. *Q. J. R. Meteorol. Soc.*, **108**, 407–426
- Smith, R. N. B. 1990 A scheme for predicting layer clouds and their water content in a general circulation model. *Q. J. R. Meteorol. Soc.*, **116**, 435–460
- Sun, Z. and Shine, K. P. 1995 Parameterization of ice cloud radiative properties and its application to the potential climatic importance of mixed-phase clouds. *J. Climate*, **8**, 1874–1888
- Wylie, D., Pironen, P., Wolf, W. and Eloranta, E. 1995 Understanding satellite cirrus cloud climatologies with calibrated lidar optical depths. *J. Atmos. Sci.*, **52**, 4327–4343
- Young, K. C. 1993 *Microphysical processes in clouds.* Oxford University Press